

Beyond the Born Approximation: A Precise Comparison of e^+p and e^-p Elastic Scattering in CLAS

A Proposal to PAC31

J. Arrington*, L. El Fassi, K. Hafidi, R. J. Holt, P. E. Reimer
Argonne National Laboratory

F. Klein, D. Sober
The Catholic University of America

K. Joo*, M. Ungaro
University of Connecticut

B. A. Raue*, W. Boeglin, M. Moteabbed
Florida International University

A. Afanasev*, W. K. Brooks*[†], V. D. Burkert, A. Deur, L.
Elouadrhiri, D. W. Higinbotham, B. A. Mecking, W. Melnitchouk
Jefferson Lab

J. Lachniet, M. Niroula, L.B. Weinstein*, G.E. Dodge, C.E. Hyde-Wright, H. Juengst, S. Kuhn
Old Dominion University

X. Zheng
University of Virginia

and the CLAS COLLABORATION

(Dated: December 11, 2006)

A direct measurement of the two photon exchange contribution to lepton-proton elastic scattering is proposed. This process is expected to explain the discrepancy observed between two methods of measuring the proton's G_E/G_M ratio. A definitive test of this assertion is possible via a high precision comparison of e^+p and e^-p elastic scattering. The proposed measurement, which uniquely exploits the large acceptance of CLAS, may also influence the interpretation of other high-precision measurements including extractions of the small amplitudes in the N to Δ transition or the elastic form factors of few-body nuclei.

* spokesperson

[†] contact person

Contents

| | |
|--|-----------|
| I. Prologue for PAC 31 | 3 |
| II. Introduction | 4 |
| III. Scientific Motivation | 6 |
| A. Overview | 6 |
| B. Estimates of TPE effects | 8 |
| 1. Calculations | 8 |
| 2. Phenomenological estimates | 9 |
| C. Radiative Correction Details | 10 |
| IV. Experimental Method | 11 |
| A. Overview | 11 |
| B. Results of Beam Tests and Simulations | 12 |
| C. Description of experimental equipment | 13 |
| D. Flux Measurement and Monitoring | 17 |
| E. Triggering | 19 |
| F. Data Analysis | 21 |
| 1. Reconstruction of existing CLAS data | 22 |
| 2. Suppression of πp and $\pi\pi$ Photoproduction Backgrounds | 27 |
| 3. Reconstruction of Monte Carlo simulation | 27 |
| 4. Identification of $e^\pm p$ elastic events from g11 | 30 |
| 5. Test Run Data Analysis | 31 |
| G. Backgrounds | 35 |
| 1. Electromagnetic background from beamline components | 35 |
| 2. Hadronic background from the photon blocker | 37 |
| 3. Tagger-related background | 38 |
| 4. Møller/Bhabha electrons | 41 |
| H. Experimental Luminosity | 44 |
| I. Systematic errors | 45 |
| J. Rate estimate | 49 |
| V. Beam Time Request and Anticipated Results | 53 |
| VI. Experiments with Similar Physics Goals | 54 |
| VII. Conclusions | 56 |
| References | 56 |

I. PROLOGUE FOR PAC 31

An earlier version of this proposal was submitted to PAC 26. The result of that submission was a scientific rating of A-, a beamtime allocation of 5 of the requested 35 days to be used for test runs, and concerns expressed about the backgrounds that may be associated with the blocking of the photon beam (which was proposed as a part of producing the lepton beam), and about the differences in the experimental acceptance for the two lepton species.

Since that time, a vigorous program of test runs, data analysis, and simulation has been carried out. The concern over the background from the photon blocker has been addressed both by test runs and by a massive new GEANT4 simulation. These new simulations have gone well beyond 'proposal quality' and are clearly in the class of tools for final experiment design. The most recent, two-week-long test run used an experimental configuration which was very close to the ultimate one, including a positron/electron beam line with a 3-magnet chicane, photon blocker, lepton profile monitor, and a liquid hydrogen target. The promised beam of positrons and electrons was successfully produced and characterized, and many elastic scattering events were observed from both lepton species. Extrapolation of luminosity from this test run to the full experiment can thus be performed with a high degree of confidence.

All of the new information has validated the outcome of the original extensive simulations with GEANT3 and EGS4: the background from the photon blocker is simply not an issue. Similarly, the effects of detector acceptances have been re-evaluated and found to be controllable: a cut on the minimum lepton angle of 25 degrees results in nearly identical acceptances for the two lepton species, while maintaining the epsilon coverage from 0.1 to 0.9. Any remaining small lepton acceptance effects can be averaged away by reversing the torus field, which will perfectly interchange the acceptance of the positron and electron.

The relative levels of neutron and photon backgrounds have been quantified by the use of liquid scintillator neutron detectors with pulse shape discrimination and corroborated with dosimeter measurements at over two dozen locations within Hall B. These measurements are in agreement with the simulation results: neutrons are not a problem.

In addition to validating the original background calculations for the photon blocker, the test runs and the new simulation work of the past 30 months showed that the existing Hall B bremsstrahlung tagger beamline was the dominant source of background. This background was dramatically reduced by a months-long effort to remove background sources (massive material too close to the beamline) and to shield as much of the tagger beamline as possible with a massive new bunker (rather than with simple line-of-sight shielding walls).

While the proposal has been updated in a number of places to reflect the progress since PAC26, the original experimental approach is the same. After a tremendous amount of work and discussion, the original proposal ideas have been validated, and new insights into the backgrounds in the existing hall have been gained.

Meanwhile, little progress has been achieved toward the physics goal of explaining the factor of three discrepancy between two measurements of the electric form factor of the proton, one of the most basic quantities in all of electromagnetic nuclear physics. This issue is without question one of the most urgent and important problems in this field. It is a bold statement, but nonetheless indisputable: the proposed experiment provides the only definitive method for evaluating whether or not two photon exchange explains that discrepancy.

II. INTRODUCTION

The electromagnetic form factors are essential pieces of our knowledge of nucleon structure. However, measurements of the proton electric form factor, G_E , using different techniques differ by a factor of three at $Q^2 = 5.6 \text{ GeV}^2$ [1–6]. Until the cause of the discrepancy is fully understood, the uncertainty in the form factors affects the theoretical and experimental understanding of several measurements.

Theoretically, it is unclear what value of G_E should be used to compare to lattice calculations or models of proton structure. Theoretical corrections needed to resolve the G_E discrepancy may also be important for interpreting other electron scattering measurements. Experimentally, it is unclear what value of G_E should be used as input in the analysis of experiments from $(e, e'p)$ to color transparency, especially at high Q^2 or when studying the ε -dependence. While the discrepancy in G_E is largest at higher Q^2 , there may still be significant effects even below $Q^2 = 1 \text{ GeV}^2$, where the elastic form factors are needed as input in precision measurements of nuclear structure from $A(e, e'p)$ measurements. A systematic correction that affects both G_E and G_M could be amplified in taking the difference between proton and neutron form factors, useful for comparison with Lattice QCD [7], or in combining electromagnetic form factors with parity violating measurements to extract the flavor-dependent quark contributions to the form factors [8].

The goal of this experiment is to resolve the discrepancy between the Rosenbluth and polarization transfer measurements of G_E . It is currently believed that two-photon exchange (TPE) effects are the cause of the discrepancy. We will measure $\frac{\sigma(e^-p)}{\sigma(e^+p)}$, the ratio of elastic electron-proton and positron-proton scattering, as a function of ε and Q^2 , in order to directly extract the TPE corrections to elastic scattering for $0.5 < Q^2 < 2.5 \text{ GeV}^2$. This will provide important constraints for models of the TPE effects.

The uncertainty in G_E arises from a discrepancy between Rosenbluth separations of the unpolarized cross section [1, 4, 5] and polarization transfer measurements [2, 3]. Assuming one photon exchange (first Born approximation, see Fig. 1), the cross section can be written as

$$\frac{d\sigma_B}{d\Omega} = C_B(Q^2, \varepsilon) [\tau G_M^2(Q^2) + \varepsilon G_E^2(Q^2)] \quad (1)$$

where the virtual photon polarization $\varepsilon = [1 + 2(1 + \tau) \tan^2(\theta_e/2)]^{-1}$, $\tau = Q^2/4M^2$ and C_B is a known kinematic factor. By varying ε , the Rosenbluth measurements separate R_L , which is proportional to G_E^2 , from R_T , which depends on both G_E and G_M . These measurements yield $G_E \approx G_M/\mu_p \approx G_{\text{Dipole}}$ for Q^2 up to 5–10 GeV^2 . Recent “Super-Rosenbluth” measurements, where the recoil proton (rather than the scattered electron) was detected, have confirmed the original Rosenbluth measurements with much smaller systematic uncertainties. The form factors have also been measured in polarization transfer experiments using $(\vec{e}, e'\vec{p})$. In the Born approximation, the ratio of the transverse and longitudinal recoil proton polarizations P_t/P_l is directly proportional to G_E/G_M . These experiments show a significant decrease in G_E compared to G_M as Q^2 increases, with G_E/G_M a factor of three below the Rosenbluth results at $Q^2 = 5.6 \text{ GeV}^2$.

Two-photon exchange (TPE) contributions (see Fig. 1 (e) and (f)) might be able to explain the discrepancy [9, 10]. Because the contribution of G_E to the cross section is kinematically suppressed compared to G_M for large 4-momentum transfers, $Q^2 > 1 \text{ GeV}^2$, a small (5–8%) ε -dependent TPE correction to the cross section can explain the large difference between the polarization and Rosenbluth extractions of G_E [9, 11].

If a TPE contribution to the cross section is responsible for the entire difference between Rosenbluth and polarization transfer measurements, the effect must be approximately linear in

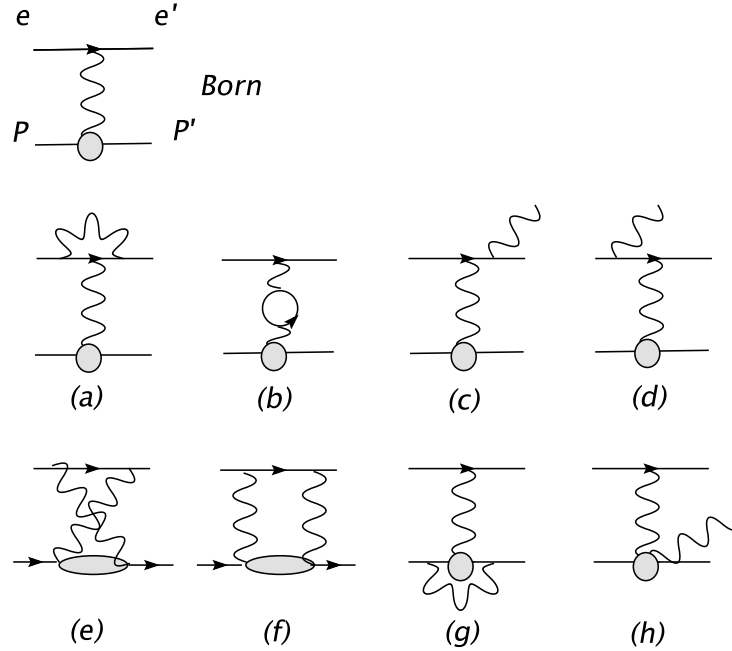


FIG. 1: Feynman diagrams for the elastic electron-proton scattering, including the 1st-order QED radiative corrections. Diagrams (e) and (f) show the two-photon exchange terms, where the intermediate state can be an unexcited proton, a baryon resonance or a continuum of hadrons.

ε [12], result in a 5–8% change in the slope of the Rosenbluth cross section plotted vs. ε , and depend only weakly on Q^2 . Figure 2 shows the values of $\mu_p G_E/G_M$ one would obtain from a Rosenbluth separation, assuming that the polarization transfer value of $\mu_p G_E/G_M$ is correct and adding a phenomenological fit to the TPE correction with a linear ε dependence and a weak Q^2 -dependence to the cross section measurements. With these simple parameterizations for the two-photon contribution, the observed slope is consistent with the Rosenbluth measurements of the form factor ratio [13] over the entire Q^2 range where data are available.

Calculations [14–18] of the TPE diagrams (diagrams (e) and (f) in Fig. 1) suggest that these effects may indeed be large enough to explain the discrepancy. However, these calculations require model-dependent treatment of the hadron structure and are therefore not yet sufficiently understood to be applied to the data as additional radiative corrections. The TPE explanation is also supported by a reexamination of positron-proton and electron-proton scattering [19]. The dominant TPE effect on the cross section comes from the interference between one-photon and two-photon exchange, which changes sign when the charge of the beam or target changes. The e^+/e^- cross section ratio data show a linear ε -dependence of $5.8 \pm 1.8\%$, with the largest effects at small ε . However, there are only seven data points at $\varepsilon < 0.5$ and only one of those is at $Q^2 > 1 \text{ GeV}^2$. In addition, the statistical errors are typically at least 5%.

We propose to extend these e^+/e^- cross section ratio measurements to low ε and moderate Q^2 values with high statistical precision. We will use a 5.7 GeV electron beam incident on the CLAS tagger to create a real photon beam. The photon beam will strike a converter, creating e^+/e^- pairs which enter a 3-dipole chicane. These pairs will be separated from the photon beam by the first dipole magnet; the photon beam will be stopped by a photon blocker in the

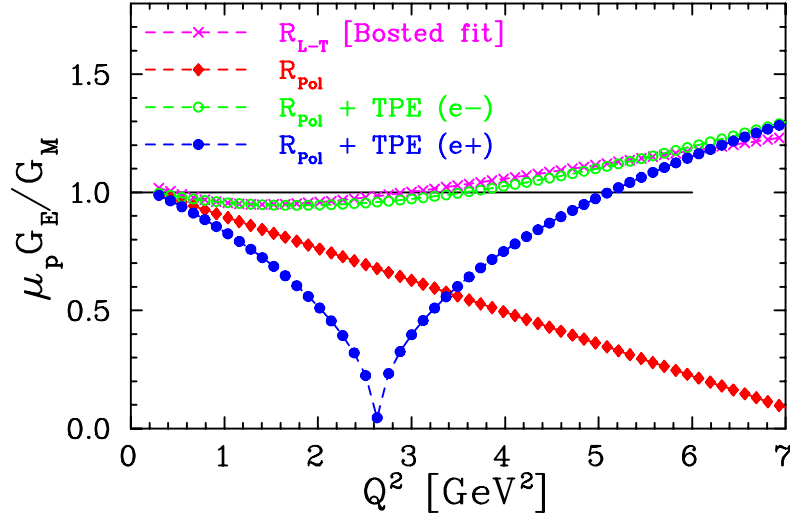


FIG. 2: The value of $\mu_p G_E/G_M$ that would be measured in a Rosenbluth separation under various assumptions for the TPE contributions. The red diamonds show the results of the Rosenbluth measurement if there are no TPE effects, based on the form factor ratio from the polarization transfer experiments. The green open and blue closed circles show the results of the Rosenbluth measurement for electrons and for positrons, respectively, assuming a simple parameterization of TPE corrections designed to reproduce the electron measurements [13] (crosses). Note that the difference between electron and positron measurements becomes significant even at low Q^2 values, and the effect of TPE on the positron measurements means that the slope of the Rosenbluth plot goes *negative* around $Q^2 = 2.6 \text{ GeV}^2$, meaning that above this value, one finds a negative value for $(\mu_p G_E/G_M)^2$, and thus an imaginary ratio for G_E/G_M .

second dipole; and the lepton beams will then be recombined by the second and third dipole magnets, and will proceed to impinge on a single hydrogen target in the center of CLAS. We will then detect the recoil protons and the scattered leptons in the CLAS spectrometer. In order to reduce systematic errors, we will periodically flip the polarity of the e^+/e^- magnet chicane and of the CLAS toroidal magnet. By doing this, we will simultaneously measure the cross section asymmetry for e^+ and e^- scattering from the proton to determine the magnitude of two-photon exchange effects with high statistical and systematic precision.

Since two-photon exchange could change the measured value of G_E by a factor of three, an experimental determination of its contribution becomes very important. The proposed measurements will allow us to determine the effects of TPE on electron-proton elastic scattering and resolve the ambiguity presently surrounding the charge form factor of the proton.

Section III will discuss the theoretical considerations in more detail and section IV will present the experimental method.

III. SCIENTIFIC MOTIVATION

A. Overview

The Rosenbluth formula for elastic ep -scattering [20] was derived using the one-photon exchange approximation. Measurements of nucleon electromagnetic form factors and experiments on parity-violating electron scattering are based on the same approximation. When electron

scattering data are analyzed, radiative corrections must be applied to take into account higher-order processes. These processes include vertex corrections (a and g in Fig. 1), vacuum polarization or loop diagrams (b), the emission of a real photon from the electron or proton (c,d,h), two-photon exchange (e and f), as well as higher-order (multi-photon) terms. Many of these corrections involve only lepton-photon vertices (electron bremsstrahlung, electron vertex, and loop diagrams), and can be calculated exactly in QED or, in the case of quark loops, determined from $e^+ - e^-$ annihilation data. Terms that involve the proton include the proton vertex correction, two-photon and multi-photon exchange, and proton bremsstrahlung. These terms cannot be calculated exactly and must be estimated or measured by other techniques. Of these terms, the greatest uncertainty is associated with the two-photon exchange. The proton vertex correction is quite small except for extremely high Q^2 and ϵ -independent at fixed Q^2 , while proton bremsstrahlung is fairly well understood due to a low-energy theorem. Exchange of more than two hard photons is a higher order process, and is expected to be another order of α_{em} smaller than the two-photon and other radiative correction terms.

Two-photon exchange effects, referred to as ‘dispersive effects,’ have been seen before in electron scattering on heavier nuclei. They showed up typically in the energy dependence of form factors measured in elastic electron scattering [21] and in discrepancies between nuclear charge radii measured with muonic atoms and with elastic electron scattering [22]. They were studied in several different ways, including ‘forbidden transitions’ in electron scattering (e.g.: $^{16}\text{O}(e, e') 0^+ \rightarrow 0^-(10.9) \text{ MeV}$ [23]), and the comparison of electron and positron elastic scattering from ^{12}C [24]. However, it was generally assumed that these few-percent effects would be much smaller on the proton ($Z = 1$) than on larger nuclei ($Z \gg 1$). While there have been measurements of TPE effects in the beam normal asymmetry measured in electron scattering with transversely polarized electrons [25, 26], these are observations of cross section asymmetries at the 10^{-5} – 10^{-4} level, compared to the much larger ($\sim 5\%$) effects needed to reconcile the polarization transfer and Rosenbluth separation measurements.

The formalism developed by Mo and Tsai [27, 28] is commonly used to apply radiative corrections. However, these corrections include only the infrared divergent contributions from the two-photon exchange diagrams (necessary to cancel the IR-divergent terms in the interference between proton and electron bremsstrahlung), and neglect contributions from multiple soft photon exchange (Coulomb corrections). The TPE contributions are of $\mathcal{O}(\alpha_{em})$ with respect to the Born amplitude, and are therefore important to include, especially for Rosenbluth form factor measurements that require a high-precision extraction of the ϵ -dependence of the cross section. These terms cannot be calculated in a model-independent way, and so direct measurements of such corrections must be made to allow unambiguous interpretation of electron-proton scattering measurements with an accuracy better than 1%.

Fortunately, the contribution of two-photon exchange can be measured directly without referring to models of nucleon structure. This is possible due to the fact that the TPE corrections have opposite signs for scattering cross sections of positrons vs. electrons, producing a measurable charge asymmetry in $R = \sigma(e^+)/\sigma(e^-)$, where $\sigma(e^+)$ and $\sigma(e^-)$ denote elastic cross sections of positron- and electron-proton scattering, respectively.

The radiative corrections for electron and proton scattering are discussed in more detail in Section III C. However, the radiative corrections can be divided into two categories: those whose sign is independent of charges of the incident particles, and those whose sign depends on the charges of the particles. The “standard” radiative corrections are all independent of the sign of the lepton, except for the interference term between electron (positron) bremsstrahlung and proton bremsstrahlung that is regularized by a corresponding infra-red term from TPE. The effects of TPE have the opposite sign for electrons and positrons. Therefore, after applying the standard radiative corrections, including the interference between electron and proton

bremsstrahlung, the TPE radiative correction to the cross section can be written as

$$\sigma(e^\pm) = \sigma_{Born}(1 \mp \delta_{2\gamma}), \quad (2)$$

where $\delta_{2\gamma}$ is a TPE correction. This yields a charge asymmetry of:

$$R = \frac{\sigma(e^+)}{\sigma(e^-)} \approx 1 - 2\delta_{2\gamma}. \quad (3)$$

Thus, it is evident that the charge asymmetry of Eq. 3 is a direct and model-independent measure of the TPE effect for the elastic electron-proton scattering.

B. Estimates of TPE effects

1. Calculations

Extending earlier work by Maximon and Tjon [29] on the nucleon elastic contribution to the box diagram (diagrams (e) and (f) in Fig. 1), Blunden, Melnitchouk and Tjon [14] included form factors in the loop integrals to estimate the impact of hadronic structure on the two-photon exchange calculation. Using simple monopole form factors, the structure effects were found to give rise to a significant ε -dependence, which accounted for about half of the difference between the Rosenbluth and polarization transfer measurements. With the use of realistic form factors, the effect was found to increase somewhat [18], making the discrepancy even smaller. In addition to the nucleon elastic contribution, one expects excitation of nucleon resonances, such as the Δ , to become relatively more important at higher Q^2 values, and these are currently being evaluated [18].

The Axial-VMD model, originally proposed by Drell and Sullivan [30], was recently revised by Afanasev [31]. In this model, the entire strength of the TPE effect is attributed to exchanges of axial mesons such as $a_1(1260)$ and $f_1(1285)$, which are the lightest mesons whose coupling conserves electron helicity and has the positive charge parity of the 2-photon exchange. The axial meson coupling was obtained from a fit to the difference between Rosenbluth and polarization measurements of the ratio G_E/G_M . This model predicts corrections that are small at large ε , but which can become significant at low and moderate ε values.

A calculation at the quark-parton level in the factorized approximation was performed by Afanasev, Brodsky, and Carlson [31]. It does not use any fitting parameters, and assumes a fixed value $\langle x \rangle = 1/3$ for the fraction of (longitudinal) momentum of the nucleon carried by the struck quark. Like the Axial-VMD fit, it brings Rosenbluth and polarization data on G_E into qualitative agreement, but its dependence on the electron scattering angle (or ε) at fixed Q^2 is rather different. This calculation yields a nearly linear ε -dependence over most of the ε range, that results in about the same correction to the Rosenbluth slope as the model [14], but predicts larger effects for smaller values of $\varepsilon < 0.2$. The TPE effect in this model is Q^2 -independent.

It is interesting to note that the quark-parton models of the TPE effect predict a negative sign of the charge asymmetry at large values of ε and a change of sign to positive values around $\varepsilon = 0.4$ to 0.6 . On the other hand, the models using only hadronic degrees of freedom, *i.e.*, the elastic contribution [14] and Axial-VMD [31] do not predict a change of sign as a function of ε .

Figure 3 shows the high Q^2 SLAC data on charge asymmetry [32] plotted against the predictions of the models described above. All of these models yield TPE corrections that improve the agreement between the Rosenbluth and polarization extractions of the form factors. They all predict a relatively weak dependence on Q^2 , at least for large Q^2 values, but they predict

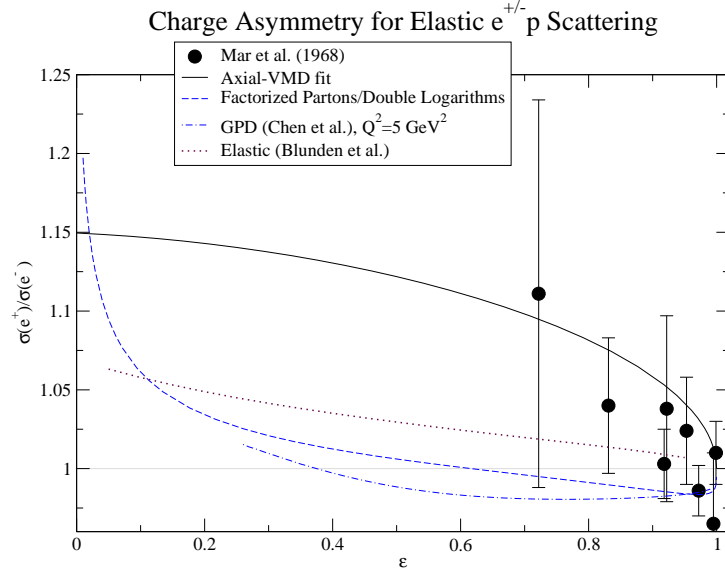


FIG. 3: The ratio of the e^+p differential cross section to the e^-p differential cross section as a function of ε .

different dependences on the electron scattering angle (or ε) at fixed Q^2 values. Therefore the proposed measurement, besides giving a definite answer to the problem of the discrepancy between Rosenbluth and polarization data, will also constrain the models of TPE effects that depend on nucleon structure.

2. Phenomenological estimates

These calculations give us some guidance as to the size and form of the TPE corrections. However, they yield different quantitative results and some are not expected to be valid at low Q^2 values. Therefore, we also try and estimate the size of expected TPE effects at low Q^2 by analyzing the Q^2 -dependence of the discrepancy itself, as well as the existing positron data at low Q^2 .

Guichon and Vanderhaeghen [9] parameterized the two-photon exchange (TPE) amplitude in the most general form and fitted the discrepancy between polarization transfer and Rosenbluth measurements in order to evaluate the magnitude of the largest contribution of the TPE terms. They discussed the possible angular dependence of the correction and concluded that the TPE effect is up to about 3.5% at the amplitude level. Their analysis predicts a cross section dependence that is approximately linear with ε , and which yields an ε -dependence to the electron cross section of ~ 3 –5% and thus a 6–10% effect on the positron to electron ratio in the Q^2 range of this proposal.

A more detailed analysis [10], using the same generalized form factors but including constraints from the positron data, allows the extraction of additional TPE amplitudes. These additional amplitudes have smaller effects on the discrepancy but are still important in the cross section and positron-to-electron comparisons. The two-photon amplitudes are extracted from a fit to the Rosenbluth/polarization-transfer discrepancy, with the constraint that the effect on the cross section be small for $\varepsilon \rightarrow 1$ where the existing positron data set reasonable

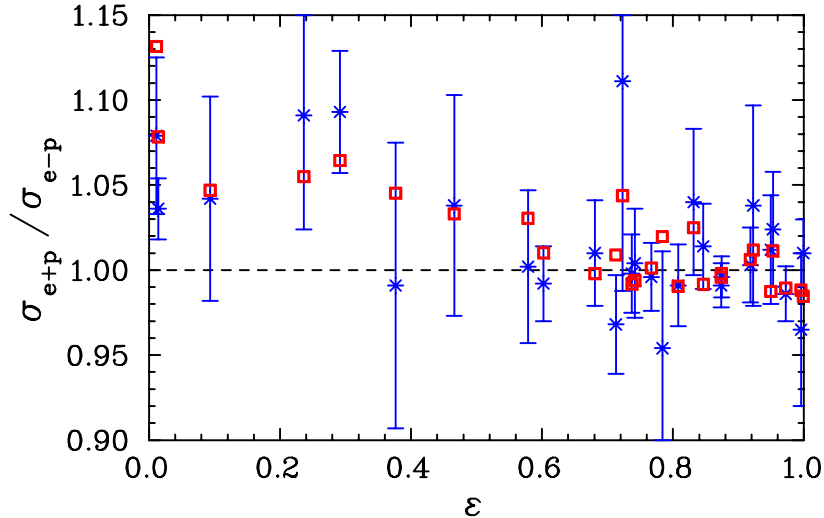


FIG. 4: The existing $\sigma(e^+)/\sigma(e^-)$ data (blue ‘x’) compared to the predicted value based on the two-photon amplitudes extracted as described in the text (red squares).

limits on the TPE effects.

Once these amplitudes have been fit to the data, we can use them to predict the expected positron to electron ratio for this proposal. The uncertainties on the amplitudes, and thus the prediction, are relatively large and the amplitudes are only well constrained by the data for $Q^2 \gtrsim 1.5 \text{ GeV}^2$. However, by comparing to the existing very low Q^2 positron data, we can see that the extrapolation to low Q^2 values yields reasonable results. Figure 4 shows the existing positron-to-electron data compared to the expectation based on the above analysis. At large ε , the fit is constrained to yield $R \approx 1$. However, the lower ε data is not used to constrain the fit, and so the agreement between the data and the extracted amplitudes gives us confidence that these amplitudes provide a reasonable starting point for estimating the size of the signal that we expect to observe in this measurement.

Based on the amplitudes extracted from this analysis, we expect that for the region where we will have high statistics, the ε -dependence of the ratio will vary from $\sim 6\%$ for $Q^2 = 0.5 \text{ GeV}^2$ to $\sim 10\%$ for $Q^2 = 2.0 \text{ GeV}^2$. Hadronic calculations of the TPE correction [18] give similar results, but with a stronger Q^2 dependence, with an ε dependence of $\approx 1\%$ at 0.5 GeV^2 , but growing to 4% at 1 GeV^2 and more than 8% at 2 GeV^2 .

C. Radiative Correction Details

The extraction of the elastic form factors requires extraction of the Born cross section. This means that corrections must be applied to the measured cross sections to correct for the additional diagrams in Fig. 1, as well as higher order terms. Most of these corrections are well understood (exactly calculable in QED) and taken care of in standard prescriptions for radiative corrections [33]. Most of these terms are identical for electron- and positron-proton scattering, and so comparison of electron- and positron-proton scattering is a sensitive way to test the terms that are not as well understood theoretically. Early comparisons of electron- and positron-proton scattering indicated that the two-photon exchange terms were very small ($\lesssim 1\%$). In this comparison, the only portion of the standard radiative corrections that changes sign is the interference between electron (positron) and proton bremsstrahlung, which is well

understood, and so the test is extremely sensitive to TPE (and multi-photon) effects.

Let us demonstrate the relation of the charge asymmetry to the TPE correction to the cross section. The amplitude of elastic ep -scattering with an accuracy of α_{em}^2 can be written as

$$A_{ep \rightarrow ep} = e_e e_p A_{Born} + e_e^2 e_p A_{e.br.} + e_e e_p^2 A_{p.br.} + e_e^2 e_p^2 A_{2\gamma}, \quad (4)$$

where the electron (e_e) and target (e_p) charges are written explicitly, and the amplitudes A_{Born} , $A_{e.br.}$, $A_{p.br.}$ and $A_{2\gamma}$ respectively describe one-photon exchange, electron bremsstrahlung, proton bremsstrahlung and two-photon exchange. Note that radiative corrections such as vertex corrections and vacuum polarization do not contribute to the charge asymmetry and therefore are not included here. Squaring the amplitude in Eq. 4 and keeping the corrections up to the order α_{em} that have odd powers of electron charge, we have

$$|A_{ep \rightarrow ep}|^2 = e_e^2 e_p^2 [|A_{Born}|^2 + e_e e_p A_{Born} 2Re(A_{2\gamma}^*) + e_e e_p 2Re(A_{e.br.} A_{p.br.}^*)], \quad (5)$$

where the notation Re is used for the real part of the amplitude.

Corrections that have an even power of electron charge, including the largest correction from electron bremsstrahlung, do not lead to any charge asymmetry. The last term in the above expression describes interference between electron and proton bremsstrahlung. Its infrared divergence exactly cancels the corresponding infrared divergence of the term $A_{Born} Re(A_{2\gamma}^*)$, making the QED description of the ep -scattering self-consistent. This interference effect for the standard kinematics of elastic ep -scattering experiments is dominated by soft-photon emission and results in a factorizable correction already included in the standard approach to radiative corrections [27, 28]. Therefore, after correcting for the interference between electron and proton bremsstrahlung, the radiative correction to the electron scattering cross section that leads to charge asymmetry comes from TPE (Eq. 5).

IV. EXPERIMENTAL METHOD

A. Overview

The experimental method proposed begins with an electron beam incident on the Hall B tagger radiator. The tagger magnet will sweep the electron beam into the tagger beam dump below the Hall B floor. The tagging detectors will not be used at all, except possibly for calibration runs.

The photon beam thus produced propagates through a photon collimator and then impinges on a converter that produces e^+e^- pairs. These pairs are horizontally separated by a dipole magnet, and the pairs and the photon beam propagate through a drift space and then enter a dipole magnet that has a pole gap with a wide horizontal acceptance. The photons are stopped within this magnet by a 'photon blocker' consisting of a narrow piece of tungsten in the center of the gap; the leptons pass to the left and right of the blocker. The leptons exit this magnet with a converging trajectory, and in a third dipole magnet they are brought to an approximately parallel round beam with a characteristic size of about one centimeter. This beam passes through a multi-component shielding structure to remove stray non-parallel background, and interacts with a large-diameter hydrogen target in the center of CLAS. Elastic scattering events are identified by a series of cuts such as coplanarity and correlations between polar angles and momenta. Once identified, all relevant quantities (such as incident lepton energy) can be calculated.

The systematic errors in this method are very small because of the symmetry of the reaction and the experimental apparatus. The capacity to simultaneously measure a wide range in ε is

due to the large acceptance of CLAS; large acceptance also permits the use of a beam of only a few hundred pA to achieve excellent statistical errors in a modest period of time. Control over the asymmetry in the incident flux of positrons and electrons is maintained by a specialized direct measurement at low rates, and continuous monitoring at high rates. Experimental backgrounds are present and non-negligible, but are held to a manageable level by careful placement of shielding materials in a strategy steered by numerous simulations.

The following sections contain detailed discussions of various aspects of the proposed experimental technique. We begin by summarizing what has been learned by simulations and test runs since this proposal was originally approved for 5 days of test running by PAC 26. A description of the equipment and the scheme to measure the incident flux of leptons will be followed by a description of the triggering method and data analysis. Next come discussions of experimental backgrounds and systematic errors. Finally, an estimate of counting rates will be given, and an approach to the physics analysis will be presented.

B. Results of Beam Tests and Simulations

The PAC 26 report contained concerns over non-target related backgrounds arising from the photon beamline. In order to study these backgrounds, we conducted several short beam tests in July and December of 2004 and the Summer 2005. Specifically, we looked at the backgrounds due to blocking the photon beam and due to dumping the high-intensity electron beam, as well as the effects of different shielding configurations and the nature of the background radiation produced. Guided by the results of these short test runs and subsequent simulations, We conducted a longer “engineering” test run in October of 2006 in which we had a fully functional electron/positron beam line and an extensively modified shielding configuration.

To summarize the results of the test runs:

1. We have identified large background sources that would arise using the previously proposed configuration. These backgrounds were significantly reduced in the 2006 test run.
2. Blocking the photon beam does not significantly increase the background, contrary to the concern of PAC 26.
3. A large amount of background comes from the tagger beamline but has been reduced by a factor of about 20 by removing small apertures in the beamline and significantly improving the shielding around the tagger and the tagger dump.
4. The background seen in the Region 3 (outermost) drift chambers depends on photon luminosity (beam current times radiator thickness, $I \cdot X$) and not on I or X individually.
5. Only a few percent of the background during normal running is neutrons.
6. Data on background sources from the test runs agrees well with expectations from simulations. This gives us confidence that simulations can guide further improvements to shielding and beamline configurations leading to further reductions in the background and hence further increases in luminosity.
7. In the October 2006 test run, we achieved a lepton luminosity that was 4% of the PAC 26 proposal. We can increase this by a factor of six (to 24% of proposal luminosity) by enlarging apertures in the cryotarget system. We anticipate improving this by another factor of four through further simulation and shielding.

8. Both electron-proton and positron-proton elastic scattering events have been identified in replay.
9. A one hour, high-current test was conducted in which we put 3 kW on the tagger dump. An air cooling system maintained a safe operating temperature and should allow us to reach 10 kW of power on the dump.

Each of these items will be discussed in more detail below.

C. Description of experimental equipment

The measurement is to be carried out using the CEBAF Large Acceptance Spectrometer, CLAS, in Hall B. The spectrometer and triggering system are all to be used in their standard configurations. A small facility for producing and monitoring positron and electron beams will, however, need to be constructed.

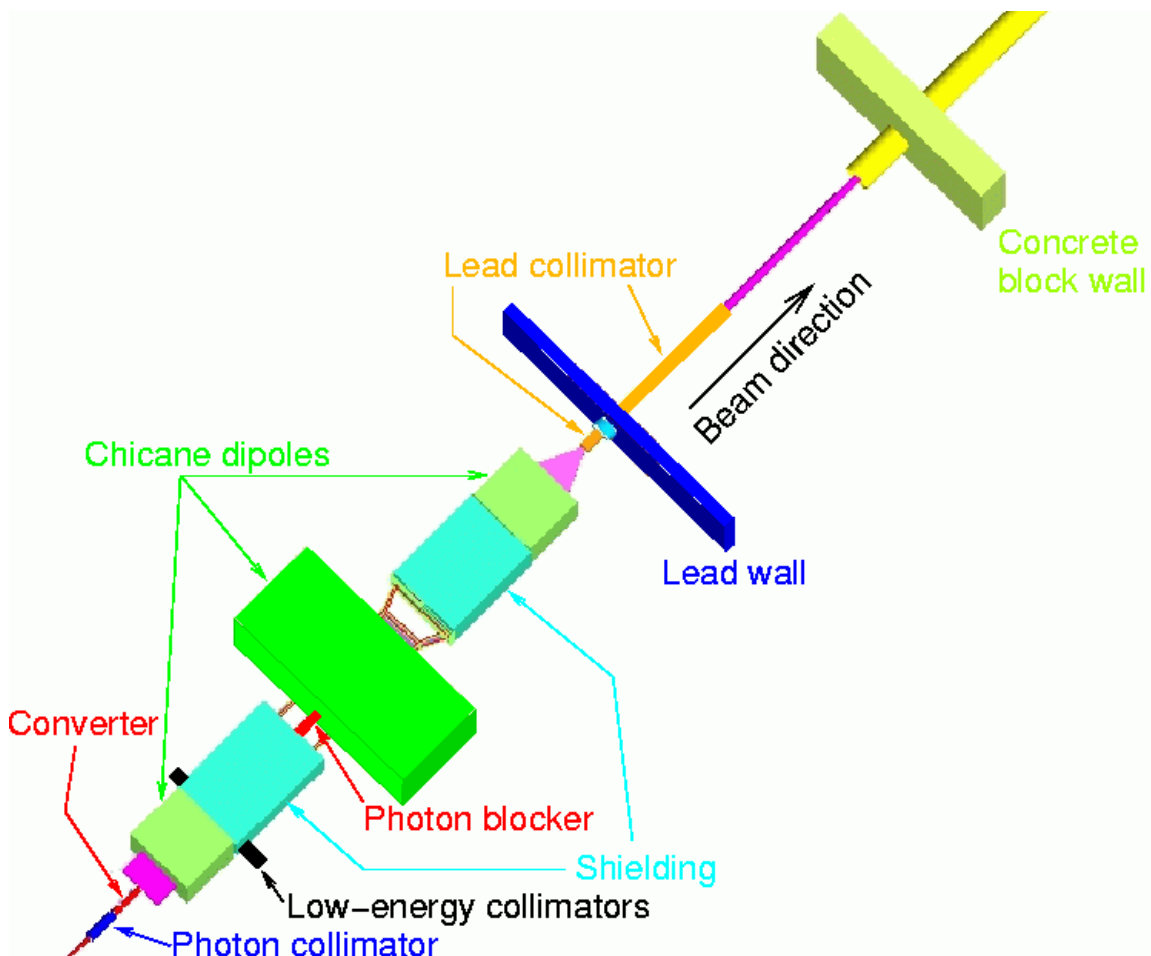


FIG. 5: An overview of the beamline devices that produce the lepton beam entering CLAS. The configuration is the same as for the October 2006 except for larger lead wall and longer lead collimator shown here. The depicted portion of the beamline is approximately 12.5 m in length.

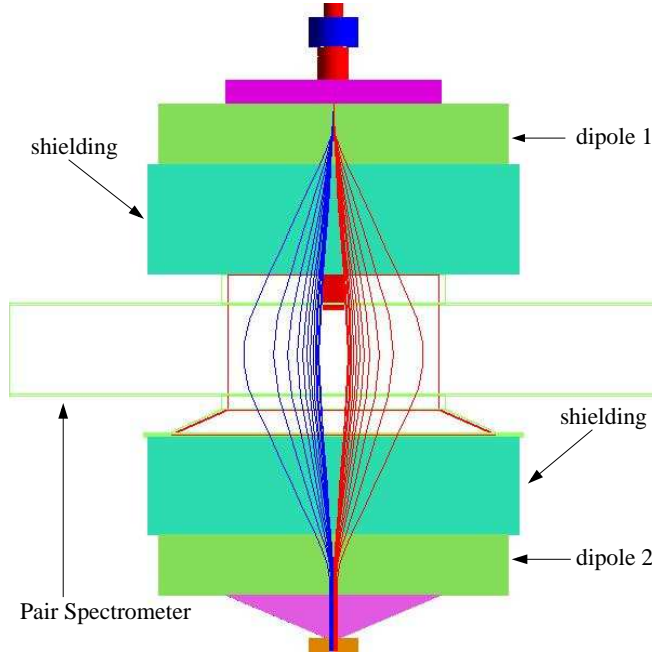


FIG. 6: Trajectories of the leptons through the chicane for the 2006 test run conditions. The scale transverse to the beamline is five times greater than the scale along the beam line. The leptons shown range in energy from 0.5 to 3.2 GeV. The two Frascati dipoles have fields of 0.42 T, and the pair spectrometer has a field of -0.385 T. Positrons trajectories are shown in blue, electrons in red. The beam enters from the top and propagates downward.

A drawing of the beamline is shown in Fig. 5. The 5.7 GeV $0.5\mu\text{A}$ electron beam from the accelerator will impinge on a 1% X_o radiator located in the conventional position in front of the tagger magnet (not shown). This magnet will deflect the primary beam to the tagger dump. (Both the beam current and the radiator thickness are significantly greater than in normal operation, therefore, use of the tagging detectors is precluded.) Although this dump has only been used for low-power deposition to date (< 800 Watts), it has been outfitted with a forced air cooling system that should allow it to reach its 10 kW design capacity. The photon beam propagates along the beamline axis, passing through an existing 12.7 mm diameter, 12 inch long nickel collimator. The initial beam energy is large to maximize Q^2 ; it has the additional benefit that the natural divergence of the photon beam is minimized, so that less collimation is required.

The collimated photon beam then passes through a 5% X_o converter, producing electron-positron pairs. The combined lepton-photon beam enters a chicane consisting of three dipole magnets, which is shown in an expanded view in Fig. 6. (A typical chicane has four dipoles. This design combines the two middle dipoles into one physical magnet.) The first and third chicane magnets are the so-called Frascati dipoles, with a 0.2 m aperture, a 0.34 m long pole face, and a maximum field of 1.2 T. The middle chicane magnet is the Pair Spectrometer (PS) Dipole with a 0.5 m aperture (0.4 m within the vacuum box), a 1 m long pole face, and a maximum field of 1.9 T. The wide aperture of the PS dipole is crucial for the experimental acceptance.

The chicane serves to spatially separate the positron and electron beams and then recombine

them. In the region where the beams are separated, the remaining photon beam is absorbed in a “photon blocker”, a 4-cm wide, 10-cm high, 20-cm long tungsten block. Either lepton beam can also be fully or partially blocked by moving in one of two “low-energy collimators”. When the low-energy collimators are partially inserted, they serve to remove the lower-energy component of the lepton beams, so as to limit the luminosity at energies that are too low to be of interest. The photon blocker can be seen at the entrance to the second magnet of the chicane in Figs. 5 and 6 as a small red rectangle, while the low-energy collimators are indicated by larger black rectangles at the exit of the first magnet.

The energy acceptance of the chicane is 90%, e.g.: from 0.5 to 5 GeV. This comes from the ratio of the Pair Spectrometer magnet aperture (40 cm) to the the photon blocker width (4 cm). If the trajectory of a 5 GeV lepton is displaced by 2 cm, then the trajectory of a 0.5 GeV photon will be displaced ten times more or 20 cm. This is well matched to the experimental requirements, since there are very few leptons with $E > 5$ GeV and we do not need the leptons with $E < 0.5$ GeV. We can, however, reduce this range using the low energy collimators. We can also shift the accepted range by changing the magnetic fields of the chicane.

During flux measurements, the low-energy blockers will be moved in to block all of the electrons, or alternatively all of the positrons, to study the energy dependence of the flux of each separately. The flux will be measured just upstream of the target location, and also monitored continuously in front of the second dipole in the chicane. Flux monitoring is described in detail in Sec. IV D.

The October 2006 test run verified the functionality of the chicane. During the test we inserted one of the low-energy collimators, blocking one of the lepton beams. We then scanned the first and third magnet currents in unison, holding the middle magnet current fixed, and monitored the beam spot with a scintillating fiber detector located at the entrance to CLAS. We then switched to blocking the other lepton beam and repeated the magnet scan. The result of the scan (shown in Fig. 7) enabled us to determine the chicane magnet settings that optimize the centering and overlap of the lepton beams. We were also able to determine that the beam spot size for all energy leptons at the fiber detector was approximately 1.9 cm (FWHM) in diameter, in good agreement with simulations. With additional collimation suggested by simulations, the spot size at the target will be only slightly bigger; 2.1 cm (FWHM). Lower energy leptons have a slightly larger spread while higher energy leptons have a slightly smaller spread. This is shown in Fig. 8.

Following the chicane is a lead shield wall with a small tungsten collar with a 5 cm inner diameter in the center. Simulations have indicated that an outer diameter of 2 m is sufficient to block most of the background generated upstream. A more challenging component to remove are the leptons with a trajectory that is similar to the lepton beam. These primarily come from scraping off the low-energy collimators, although they can come from elsewhere as well. Simulations have shown that these have wider angular dispersion and typically have energies of 100–200 MeV. Therefore, a long ‘snout’ shield follows the lead wall. We expect the inner portion of the snout to be made of carbon, to take advantage of dE/dx losses without inducing further showers, while the outermost portion will be made of lead.

During the test run, there was a 3-cm aperture collimator followed by a 10-cm thick, 1 m^2 lead wall. We varied the collimator aperture and installed various clean-up collimators during the test run. These tested configurations, in combination with simulations, will guide our final design of the wall plus snout shielding.

A single cryotarget will be used. Because of the beam divergence, the target will be larger in diameter than what is normally employed for electron beams. The outgoing lepton beam has an angular divergence that is due to a combination of the bremsstrahlung process, the pair production process, and multiple scattering in the converter and radiator. Simulations have

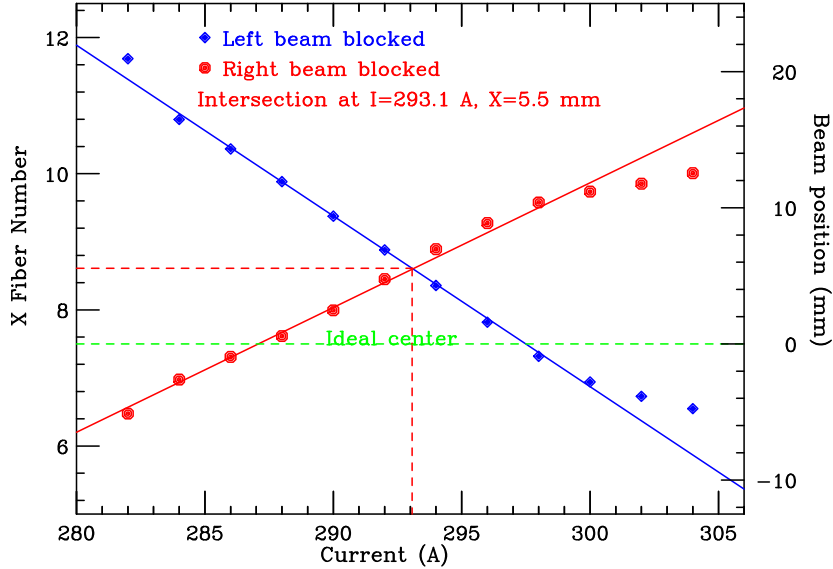


FIG. 7: Position of the individual lepton beams as a function of the current in the first and third dipoles. Data points are measured beam centroid positions at the fiber detector and the lines are fits to points 2–10.

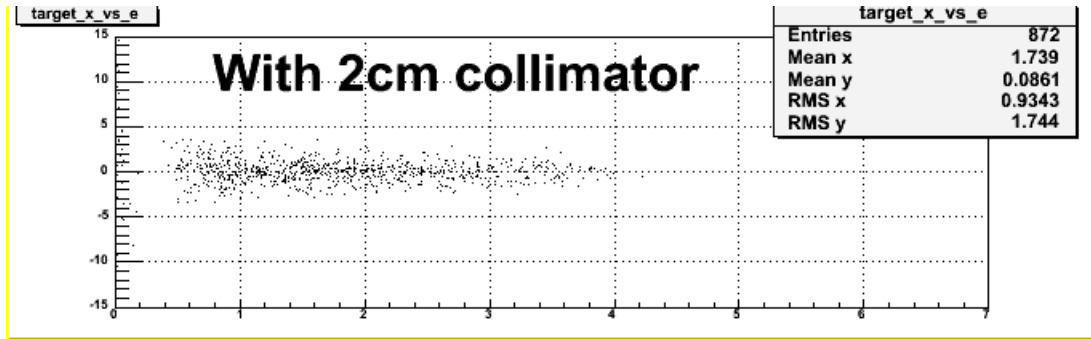


FIG. 8: Simulated beam spread perpendicular to the beam direction at the target as a function of lepton energy.

shown that the lower-momentum leptons have a somewhat broader angular distribution than the higher-momentum leptons, suggesting that multiple scattering in the converter is the most significant effect. A 10 cm diameter target will intercept all but a few percent of the leptons. This is comparable in size to targets that have been used in early photon beam experiments in CLAS, and therefore presents no new technical challenges.

However, the current heat exchangers and condensers for the cryotarget run along the beam line upstream of the target and have apertures significantly less than 10 cm. During the test run we discovered that they are one of the dominant remaining sources of background. Rebuilding them with a 10 cm aperture will reduce backgrounds in the innermost drift chambers by a factor of at least five.

D. Flux Measurement and Monitoring

Both absolute and relative measurements of the electron and positron fluxes will be performed. The relative flux will be measured continuously throughout the experiment and tied to an absolute flux measurement done prior to taking $e^\pm + p$ elastic data. The absolute flux measurement will be done by moving a position-sensitive calorimeter into the beam just upstream of the target location. Running at low beam currents, this device will enable us to measure the rate and energy distribution of electrons and positrons at the target. The flux at the target for low beam currents will be cross calibrated to the flux of unused low-energy ($E < 0.5$ GeV) leptons measured with a separate set of detectors located in the dispersed region in front of dipole 2. The flux of the unused low-energy leptons should simply scale with the primary electron beam current. Therefore, continuously monitoring this low-energy flux during the experiment should enable us to know the flux at the target for production currents.

The device we envision for the energy profile measurement at the target is a segmented lead tungstate (PbWO_4) calorimeter with a position-sensitive detector in front (see Fig. 9). The calorimeter consists of 120 crystals each with a cross-sectional area of 2×2 cm² and a length of 16 cm (18 radiation lengths). The total cross-sectional area of the calorimeter was chosen so that each electromagnetic shower that falls within the target radius (indicated by the smaller circle) deposits 99% of its energy within the calorimeter. 99% of the energy of an electromagnetic shower is contained within a cylinder of 3.5 Molière radii (R_M) centered on the incident particle [34]. R_M for PbWO_4 is 2.0 cm meaning that we need an additional 7.0 cm beyond the edge of the target, or a total diameter of 24 cm (indicated by the larger circle), in order to contain 99% of the shower. We can obtain 96% containment with a total diameter of 20 cm (indicated by the middle circle). This can be covered by 80 crystals.

The position-sensitive detector in front of the calorimeter will tell us the location of the incident particle on the face of the calorimeter. The detector will be likely be either a pair of crossed microstrip detectors or wire chambers. 1 mm position resolution is easily achievable and sufficient for our purposes. The active area of the detectors will be slightly larger than

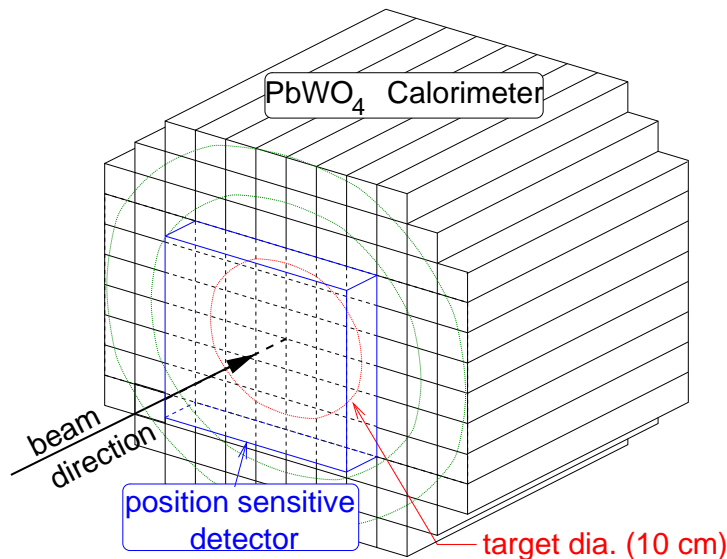


FIG. 9: PbWO_4 calorimeter and position-sensitive detector used to measure the distribution of lepton energy near the target location.

12×12 cm²—sufficient to cover an area slightly larger than the target.

Previous studies [35] have shown that an energy resolution of $\sigma_E/E < 2\%$ can be obtained for an electron energy of 1 GeV and $\sigma_E/E < 0.9\%$ for 5 GeV electrons. This was done using gain-stabilized phototubes and also required controlling the temperature of the crystals to within $\pm 1^\circ\text{C}$. We can calibrate our calorimeter by illuminating it with particles of known energy and measuring the response of each element as a function of incident particle position. The range of energies at which we calibrate will match the lepton energies of the experiment—0.5 to 5.0 GeV. The energy calibration can be done with tagged photons. A center-of-gravity technique will enable a position reconstruction to within approximately 2–3 mm[35].

The flux of unused low-energy leptons in the dispersed region in front of the second dipole will be continuously monitored. At this location, leptons with energies between 5 and 0.5 GeV are dispersed to locations between 2 and 20 cm from the central axis of the beam while leptons with an energy of less than 0.5 GeV are located beyond 20 cm. Detector placed at $x = 22$ cm in both the positron and electron beams can then be used to monitor the relative rates of positrons and electrons. Changes in the position of the lepton beams would be seen as a change in relative rates in the two monitoring detectors.

The detectors we envision for relative flux monitoring are single quartz rods Cerenkov counters—one or more in each beam—instrumented with a fast photomultiplier tube as shown in Fig. 10. Quartz has an index of refraction of 1.47 resulting in Cerenkov radiation for all electrons and positrons of interest. This index of refraction also results in total internal reflection for the Cerenkov radiation and thus excellent light collection efficiency. In addition, quartz is radiation hard [36] and should stand up well over the course of the experiment despite the high particle flux; we expect rates in these detectors on the order 10^7 Hz. With a fast PMT we should be able to count individual leptons. This is preferable to integrating PMT signals in that small differences in detector response to different charges will be minimized.

An absolute calibration of the flux monitoring detectors can be tied to the measurement of the flux at the target using the PbWO₄ calorimeter. With one of the beams blocked off, the flux at the target can be measured and compared to the rate in the monitoring detector. The roles of the beams can then be reversed and the other monitoring detector calibrated. It is likely that measurements at different beam currents will be necessary to verify scaling of the e^+/e^- fluxes. The sum of the rates in each of the quartz Cerenkov detectors will be proportional to the rate on the target. The ratio of the left and right quartz Cerenkov detectors will give us a continuous monitor of the relative e^+/e^- rates.

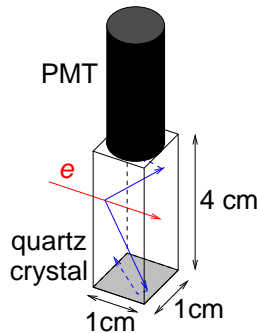


FIG. 10: Flux monitoring detector consisting of a single quartz rod and one PMT. Blue lines indicate the Cerenkov cone. The bottom surface is mirrored to improve light collection efficiency.

E. Triggering

Because the initial lepton energy is unknown, it is necessary to detect both the scattered lepton and the scattered proton to fully reconstruct an event. As such, the usual single-electron trigger employed by CLAS is not appropriate for this measurement. This trigger, based on the Cerenkov counter and electromagnetic shower calorimeter, would miss electrons and positrons at larger angles, severely limiting the coverage in ε . A further reason not to use the conventional trigger is that it may be biased by the Cerenkov counter, since that device has a slightly different efficiency for out-bending and in-bending tracks.

Instead, a trigger designed to detect $e^\pm p$ coincidences was used for the 2006 test run. This trigger required two charged tracks in opposite sectors and was constructed by requiring hits in time-of-flight counters in opposite sectors. Fig. 11 shows a cross-section of the CLAS detector with the 4 TOF panels highlighted. For a few runs, a Level 2 (drift chamber) trigger in the opposite sectors was required. The standard CLAS trigger system was adequate to fulfill these requirements.

A simple simulation was performed to determine the kinematic coverage in the (Q^2, ε) plane using the opposite sector TOF trigger. Elastic e^-p scattering events were generated at the target center for initial electron energies in the range 0.5 GeV to 5.5 GeV in 50 MeV steps. At each electron energy, electrons were elastically scattered at angles between 0 and 180 degrees in 1 degree steps. For each electron-energy/electron-angle bin, the scattered electron and scattered

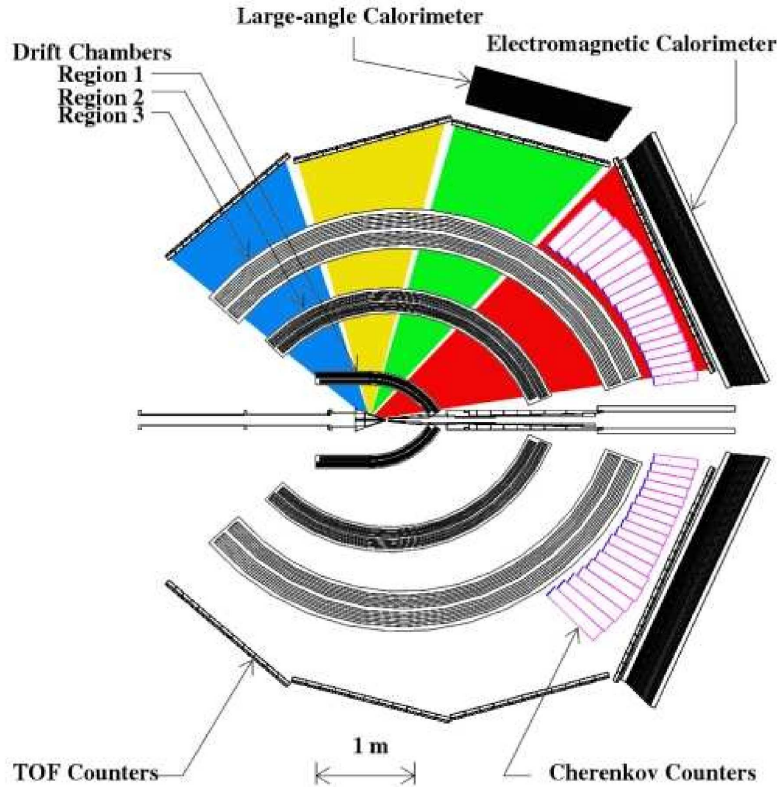


FIG. 11: A cross-section of the CLAS detector. The 4 TOF panels are highlighted in different colors: panel 1 (red) 8° - 45° , panel2 (green) 47° - 74° , panel 3 (yellow) 76° - 105° , panel 4 (blue) 107° - 141° .

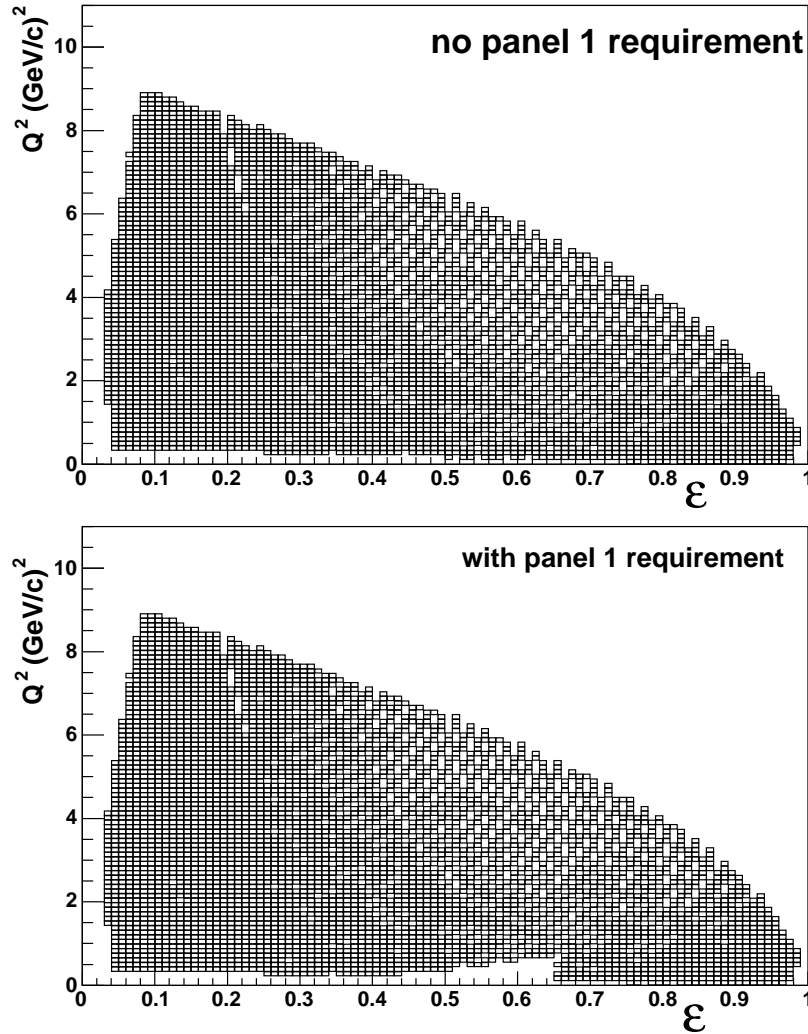


FIG. 12: The kinematically allowed region in Q^2 and ϵ for an opposite sector TOF trigger for $I_{torus}=1250$ A. The top figure has no panel-1 requirement while the bottom figure requires a hit in TOF panel-1.

proton were propagated through the CLAS torus field out to the TOF panel. Fig. 12 (top) shows a plot of the (Q^2, ϵ) values for which both the electron and proton strike a paddle in the TOF system for $I_{torus}=1250$ A. It should be noted that this is a purely kinematic simulation: not all of the allowed region in Fig. 12 will be equally populated in the real experiment. Fig. 13 shows the kinematically allowed TOF paddle number combinations in opposite sectors. The TOF panel boundaries are also shown.

Both simulation and the 2005/2006 test run results show that the TOF rates are highest on panel 4. Fig. 13 shows that in events where one of the particles of interest is detected on panel 4, the other particle of interest is never detected on panel 4. To reduce the accidental trigger rate due to uncorrelated panel-4/panel-4 coincidences, the 2006 test run used a trigger which required a hit on TOF panel 1 in one sector ($\theta < 45^\circ$) in coincidence with a TOF hit on any panel in the opposite sector. A minimum ionizing signal in the forward calorimeter was also required in the same sector as the TOF panel 1 hit. This trigger excluded a small region of the allowed (Q^2, ϵ) space. This lost coverage corresponds to throwing out the panel-2/panel-2 coincidences seen in Fig. 13. The effect of this trigger on the (Q^2, ϵ) coverage is shown in

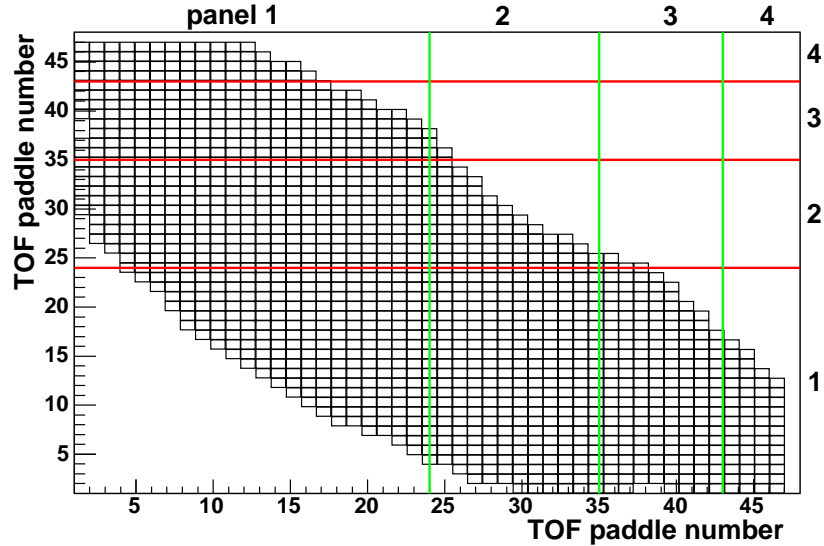


FIG. 13: The kinematically allowed TOF paddle pairs for an opposite sector TOF trigger. The TOF panel boundaries are drawn on in red and green.

Fig. 12 (bottom). The kinematic hole introduced by this trigger is small, and can be removed by extending the trigger definition to also allow events which have TOF hits on panel 2 in one sector and panel 2 in the opposite sector.

The test run trigger rate at the end of the run (after significant improvements to beamline shielding and collimation were made) was 600 Hz. However, this was dominated by noise and background since it was independent of whether or not the target was full. These backgrounds will be significantly reduced for the experiment, allowing us to increase the luminosity by a factor of at least 25 without running into DAQ rate limitations.

F. Data Analysis

Because this experiment has a tremendous spread of beam energies and will not use the standard electron identification (EC or Cerenkov counter), we need to demonstrate that we can clearly and cleanly identify elastic lepton-proton scattering events. We have done this four different ways, with existing CLAS e1c electron data, existing CLAS g11 photon data, monte carlo simulation, and with test run data containing both electron and positron scattering events. We also need to show that we can reject physics background, primarily from pions. We have done this with g1c data.

One example of how the data analysis chain might proceed is given in the following. The first criteria to be applied is to select events with only two hit-based tracks. The next requirement, that the tracks be co-planar and in opposite sectors, will strongly favor elastic scattering. Vertex times can be computed in two hypotheses for lepton/proton identification, and the correct vertex time difference will be consistent with zero. The resolution should be more than adequate to identify the lepton of the pair using this method. In addition, dE/dx in the time of flight counters (compared to the momentum from hit-based tracking) can provide further information to help identify the proton, without biasing the positron/electron selection.

Once the lepton is tentatively identified, its vertex time can be used to provide an event

start time for time-based tracking, or, alternatively, the proton can be used to provide the event start time. Once time-based tracking has been performed, one can perform a tighter $\Delta\phi$ cut to ensure co-planar kinematics. At that point, one can assume that elastic scattering is the correct process, and can then calculate the beam energy and various kinematics using any combination of two variables of measured electron and proton kinematics. By comparing the measured and calculated values, one can achieve further background reduction by cutting out unphysical events. The ultimate analysis at this stage would be to use kinematic fitting to get the most consistent set of parameters and the cleanest identification of elastic scattering. Because the charged particle *angle* measurement is almost entirely determined by the Region I drift chamber (before any bend in a magnetic field), four of the five kinematic parameters measured (of which only two are independent) are insensitive to whether the lepton is a positron or electron; thus the comparison of the two can be performed very accurately.

1. Reconstruction of existing CLAS data

To demonstrate the ability of CLAS to perform such a data selection, we performed an analysis for data from the E1C run period that were taken in 1999 with electron scattering off a proton target. We considered two data sets for this analysis. The first data set is with $E_{beam} = 1.515$ GeV and a 1500 A torus field, and the other is with $E_{beam} = 4.462$ GeV and a 2250 A torus field. In both cases, the hardware trigger was intended to identify electrons, however, there was a substantial number of events that were triggered by non-electrons, particularly at the higher energies. Note that we did not use our knowledge of the beam energy for any of the event selection described below.

To perform time-based tracking, we normally use electron hits to calculate a candidate event start time (electron software trigger). However, for this analysis, we first identify the proton candidate hit via dE/dx in the time-of-flight (TOF) scintillator counters, we assume that the track for this hit has the proton mass, and then calculate a candidate event start time (proton software trigger). The top panel in Fig. 14 shows the W distributions for 4.462 GeV data after we select events for one proton and one electron. The solid line represents the proton software trigger events and the dashed line represents the nominal electron software trigger. Any contamination will be further eliminated via elastic kinematic constraints, as shown below. The bottom plot in Fig. 14 shows that event selections with one proton and one electron in opposite sectors substantially reduce inelastic events without losing elastic events.

Once events with one proton and one electron in opposite sectors are identified, we can substantially eliminate inelastic events by applying the co-planarity cut as shown in Fig. 15. The top figure shows the difference between ϕ_e and ϕ_p for $E_{beam} = 4.462$ GeV and the bottom figure is for $E_{beam} = 1.515$ GeV. The selection of elastic ep candidates are based on the cut, $178^\circ < \Delta\phi < 182^\circ$ for this analysis.

We then analyzed the data using two different methods. In method one, we used the measured scattered electron angle, θ_e , and momentum, p_e , to calculate the incident electron energy and scattered proton momentum and angle. In the other method, we used the electron and proton scattering angles, θ_e and θ_p , to calculate the other kinematic quantities. Please note that we did not use our knowledge of the incident electron energy for either method. Fig. 16 shows the difference between the measured and calculated kinematic quantities for both methods. The top panel is for $E_{beam} = 4.462$ GeV and the bottom panel is for $E_{beam} = 1.515$ runs.

Fig. 17 shows the W spectrum before (solid line) and after (dashed line) the kinematic cuts to eliminate inelastic events. The top figure is for $E_{beam} = 4.462$ GeV and the bottom figure is for $E_{beam} = 1.515$ GeV. (Note that we used our knowledge of the incident energy to compute

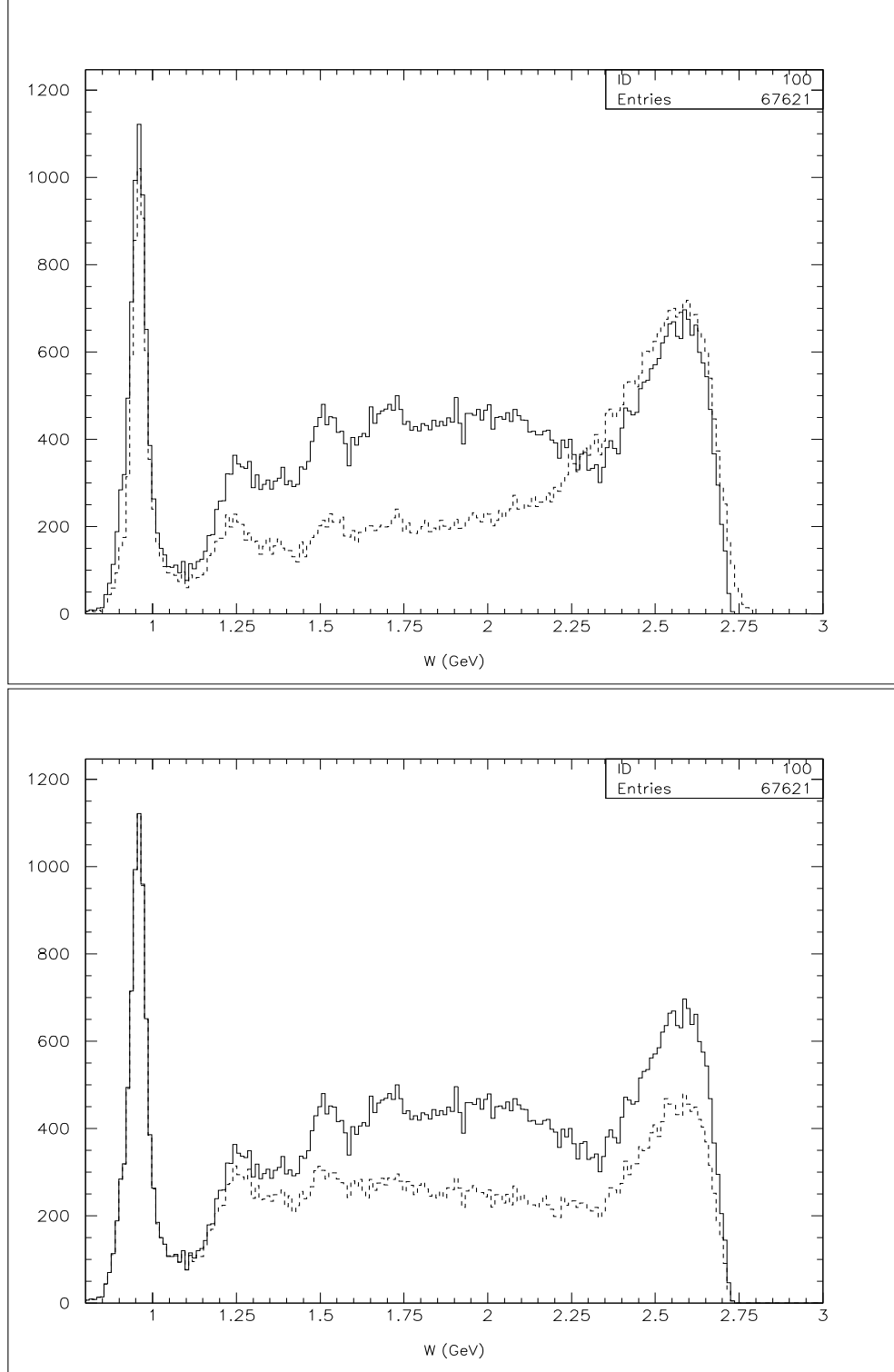


FIG. 14: W spectrum from E1C data for $E_{beam} = 4.462$ GeV after single-electron and single-proton events are selected. Top figure: Events triggered by an electron-software trigger (dashed) and or a proton-software trigger (solid). Bottom figure: Events with a proton trigger (solid) and combined with an electron in the opposite sector (dashed).

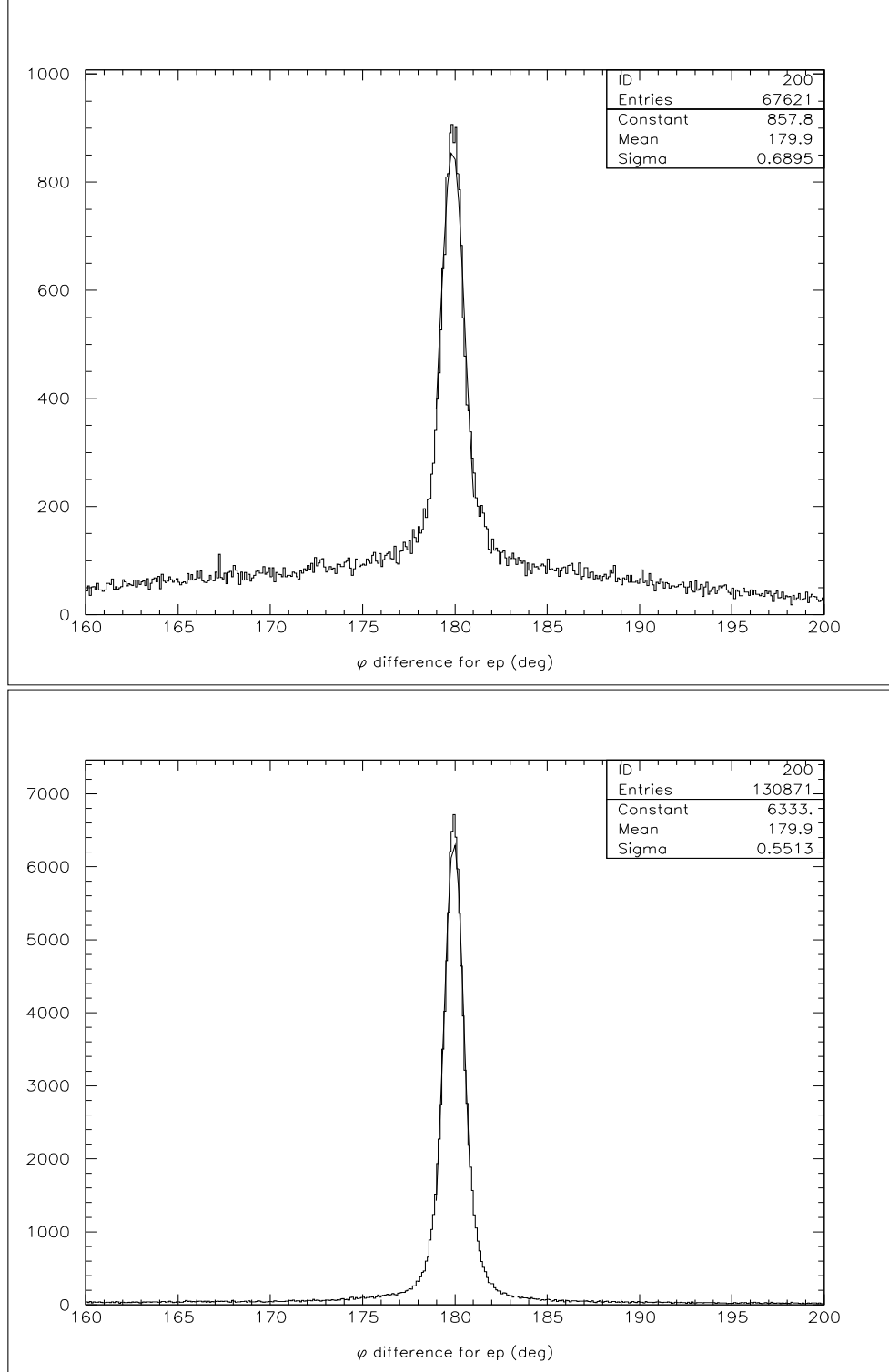


FIG. 15: ϕ difference spectrum between protons and electrons to select coplanar events. The top figure is from E1C data for $E_{beam} = 4.462$ GeV and the bottom figure is from $E_{beam} = 1.515$ GeV.

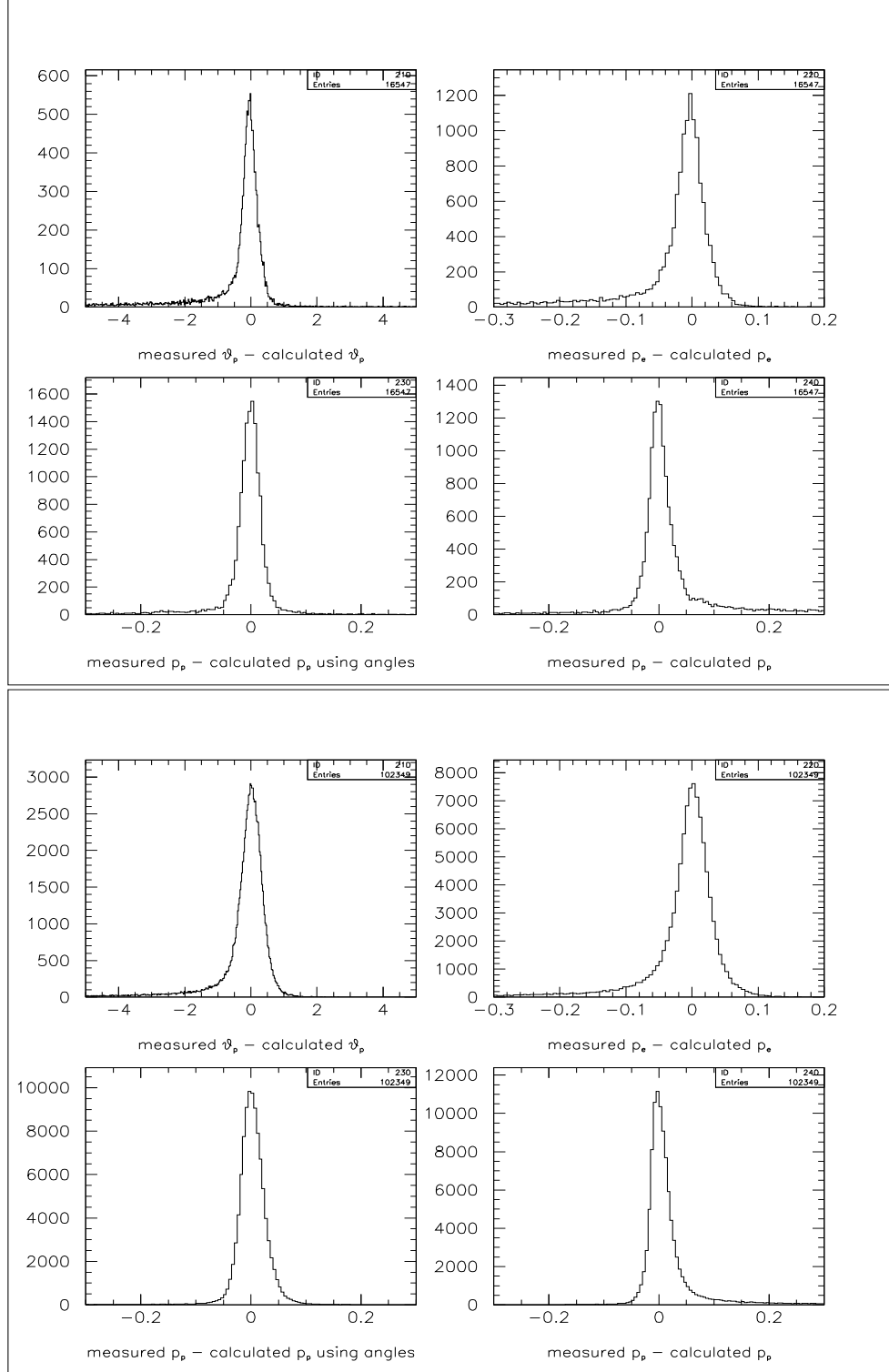


FIG. 16: Kinematic cuts using ep elastic kinematics after coplanar events are selected. Top left: difference between measured proton angle and calculated proton angle. The proton angle is calculated using the measured electron angle and momentum. Top right: the electron momentum is calculated using the measured electron and proton scattering angles. Bottom left: the proton momentum is calculated using the measured electron and proton scattering angles. Bottom right: the proton momentum is calculated using the measured electron angle and momentum. Top figure is from E1C data for $E_{beam} = 4.462$ GeV and the bottom figure is from $E_{beam} = 1.515$ GeV.

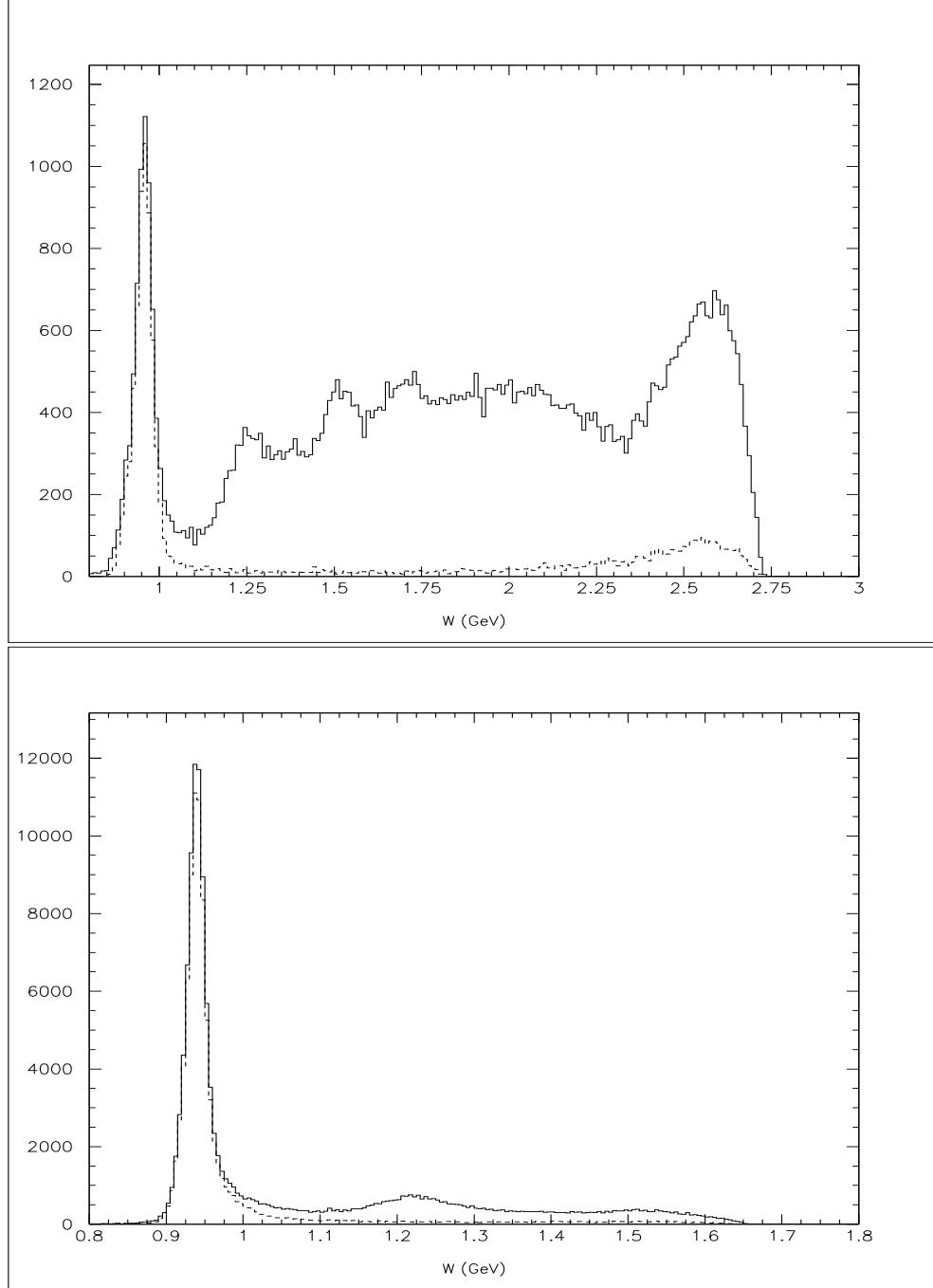


FIG. 17: W spectrum from E1C data after one-electron and one-proton events from the proton software trigger. The dashed lines represent ep elastic events after kinematic cuts were applied. The top figure is from E1C data for $E_{beam} = 4.462$ GeV and the bottom figure is for $E_{beam} = 1.515$ GeV.

W , but not to select the events plotted.) The long tail extending to large W and the peak at $W \approx 2.5$ are consistent with the radiative tail (ie: the electron radiates a photon before scattering) and would not be removed by these cuts.

This shows that we can isolate elastic scattering events in actual CLAS data even without knowledge of the incident electron beam energy.

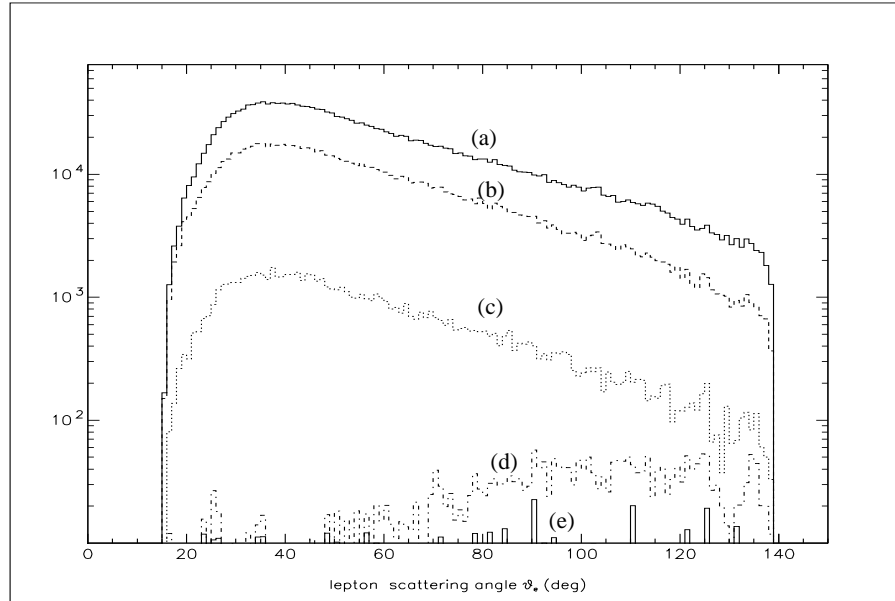


FIG. 18: π^- angular distribution for $\gamma p \rightarrow \pi^- p X$ events with $E_{\gamma}^{max} = 4.4$ GeV from the 1999 glc run. The events were analyzed as if they were ep scattering events. (a) All events, (b) events in opposite sectors, (c) coplanar events, (d) events also requiring the π^- momentum to be consistent with the electron momentum from ep elastic kinematics, and (e) events also requiring the proton momentum to be consistent with that of ep elastic kinematics. Note the almost complete elimination of this background channel.

2. Suppression of πp and $\pi\pi$ Photoproduction Backgrounds

Pion photoproduction is the other source of background from physics processes in the target. The photons come from lepton virtual bremsstrahlung. Possible background reactions include $\gamma p \rightarrow \pi^- p X$, $\pi^+ p X$ or $\pi^+ \pi^- X$ where one of the π is misidentified as a lepton or as a proton (in the case of $\pi^+ \pi^- X$). To demonstrate our ability to identify and remove these $\pi^\pm p$ and $\pi^+ \pi^-$ events, we analyzed data from the glc run period that were taken in 1999 with real photons incident on a proton target. Fig. 18 shows the angular distributions of π^- from $\gamma p \rightarrow \pi^- p X$ reaction. The top curve (a) shows the π^- angular distributions from all $\pi^- p$ events. Curves (b) through (e) show the cumulative effects of requiring (b) opposite sector events, (c) coplanar events, (d) π^- momentum consistent with ep elastic scattering and (e) proton momentum consistent with ep elastic scattering. This clearly shows that ep elastic (beam energy-independent) kinematic cuts can suppress almost all background events from $\gamma p \rightarrow \pi^- p X$. We also achieved similar suppression results for $\pi^+ p$ and $\pi^+ \pi^-$ events.

3. Reconstruction of Monte Carlo simulation

To understand resolution and acceptance issues, we performed a Monte Carlo simulation. We used the program ELAST_GEN that produces radiated elastic events, and then we used the CLAS Monte Carlo simulation program (GSIM) for a complete model of the CLAS detector system, combined with the GSIM Post Processor (GPP) to introduce realistic resolution

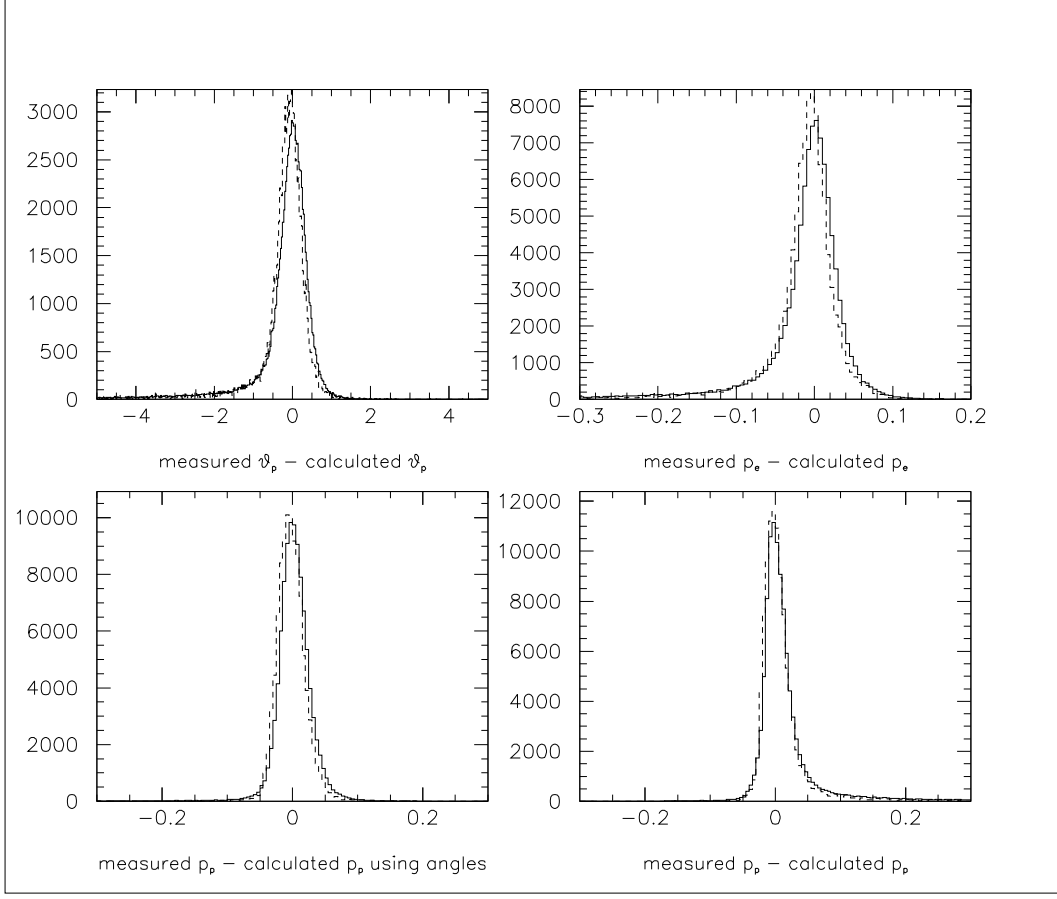


FIG. 19: A comparison of kinematic cuts between data and Monte Carlo simulation for $E_{beam} = 1.515$ GeV. The solid line is for data and the dashed line is for simulation.

effects. We reconstruct the simulated events using the reconstruction program (RECSIS) that is used to reconstruct experimental data. This simulation and reconstruction packages have been successfully used in almost all CLAS publications.

Fig. 19 shows comparisons of data with Monte Carlo simulation using kinematic cuts that select ep elastic events. These are for $E_{beam} = 1.515$ GeV. They clearly show good agreement between the data and the simulation.

We have also studied the acceptance and resolution effects between e^-p and e^+p radiated elastic events. Once we generate e^-p elastic events for $E_{beam} = 1.515$ GeV using the program ELAST_GEN, we replace e^- by e^+ to create e^+p radiated elastic events. By doing so, we can make sure that both events have the same kinematics for leptons and protons. We perform the same procedure to reconstruct both event files as described above using two different torus magnetic fields. One field is 1500 A and the other is 750 A.

Fig. 20 shows a comparison of resolutions between simulated radiated e^-p and e^+p elastic events. The top figure is for a 1500 A torus field and the bottom figure is for a 750 A torus field. The solid line is for e^+p elastic events and the dashed line is for e^-p elastic events. The resolution from e^-p elastic is slightly better than e^+p elastic. This is mainly due to different values of $\int \vec{B} \cdot d\vec{l}$ for the two trajectories. This effect can be fully studied by reversing the polarity of the torus field in simulation and experiment to minimize the systematic errors.

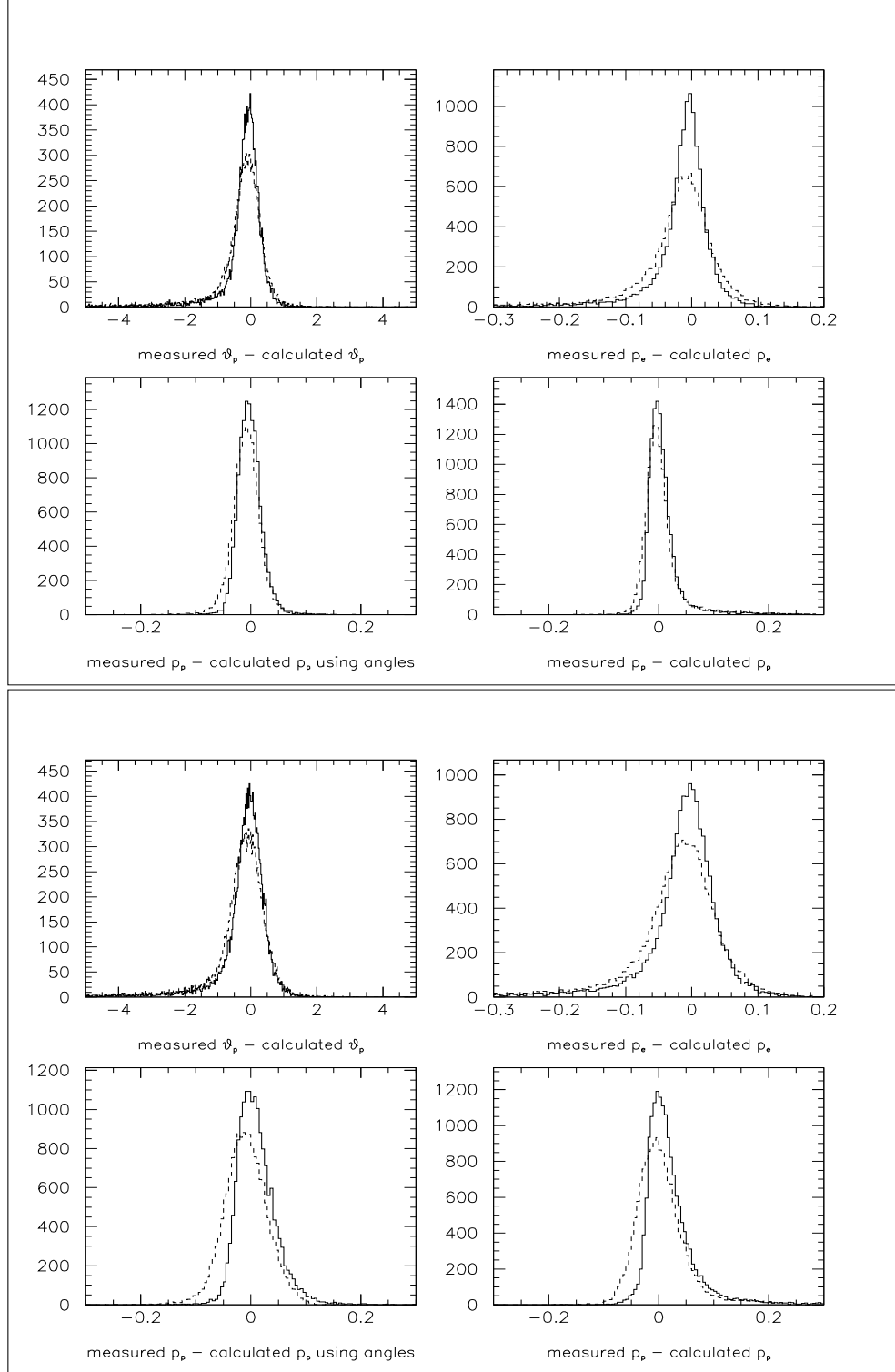


FIG. 20: A comparison of resolutions between simulated radiated e^-p and e^+p elastic events. The top figure is for 1500 Å and the bottom figure is for 750 Å. The solid line is for e^+p elastic events and the dashed line is for e^-p elastic events

4. Identification of $e^\pm p$ elastic events from g11

We analyzed data from the g11 run in order to see if we can identify ep elastic events in a photon experiment. The g11 run used a 4.0 GeV electron beam to produce a real photon beam with a 3.8 GeV endpoint energy incident upon a proton target. We looked for events with a proton and one other charged particle in opposite CLAS sectors and a calorimeter hit associated with the other charged particle. These events can come from photon pair production in the target (40 cm liquid hydrogen or 4% radiation length) or from meson production followed by e^+e^- decay. We required the calorimeter hit in order to eliminate the huge background from hadron photoproduction.

Fig. 21 shows the angle of the missing particles (Θ_X) vs. the mass squared of the missing particles for the $\gamma p \rightarrow e^\pm p X$ reaction for e^+ (top panel) and e^- (bottom panel). Θ_X corresponds to the perpendicular component of the missing momentum p_X^\perp , which can be calculated without knowledge of the beam energy. Note the isolated peak at $\Theta_X = 0$ and $MM_X = 0$. This shows that cutting on Θ_X or on p_X^\perp can isolate elastic ep events. The cleanliness of this cut is shown

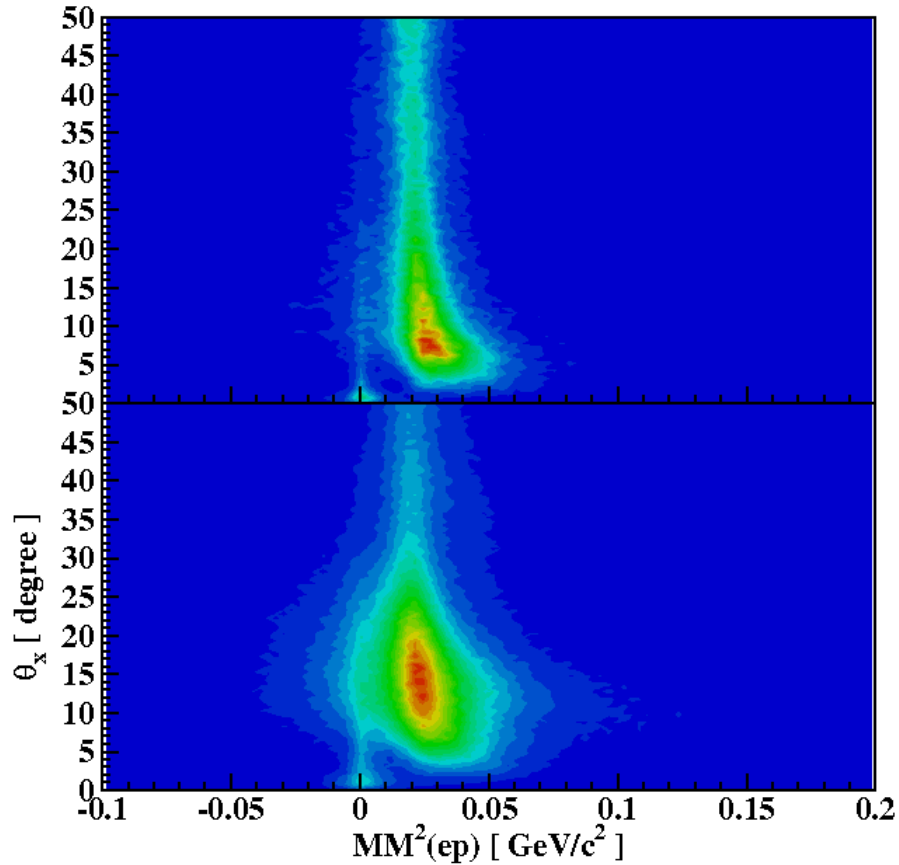


FIG. 21: Proton plus one other charged particle events from the g11 run ($\gamma p \rightarrow e^\pm p X$). The other charged particle is required to have an EC hit. The top and bottom panels are for positive and negative particles respectively. Θ_X is the angle of the missing momentum with respect to the beam. It corresponds to our proposed cuts on missing perpendicular momentum p_X^\perp . $MM^2(ep)$ is the mass (squared) of the missing particles. The isolated peak at (0,0) shows that a cut on small values of p_X^\perp cleanly selects (ep) elastic events.

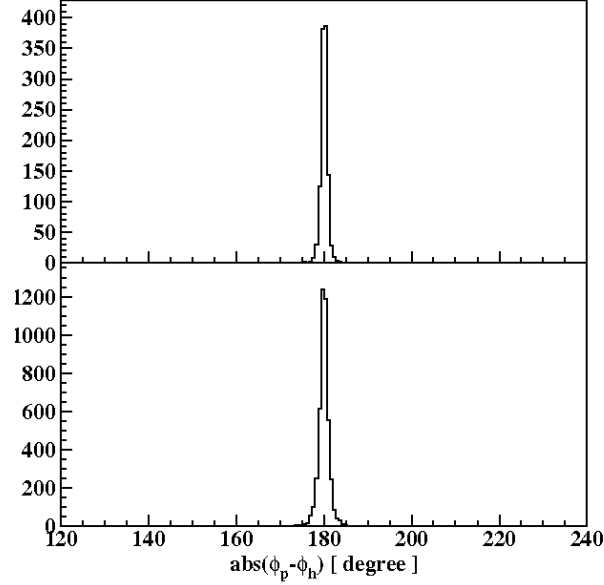


FIG. 22: $e^\pm - p$ opening angle after cutting on θ_X . Top and bottom plots are for e^+ and e^- respectively. Data from g11.

in Fig. 22 which shows the opening angle between the positron (top) or electron (bottom) and the proton.

We see about 1200 e^+p and 4000 e^-p elastic scattering events using 20% of the g11 data set. These are dominated by small scattering angle (see Fig. 23) and small Q^2 . The disparity in number is due to the difference in the acceptance at small angles (angles we are planning to cut out in our analysis). Note that there are almost zero events with $Q^2 > 1 \text{ GeV}^2$.

This analysis shows that: 1) we can identify elastic lepton-proton scattering events with a photon beam, and 2) the event rate is much too low in the standard configuration.

5. Test Run Data Analysis

The test run was conducted for three weeks in October, 2006. The 3.3 GeV electron beam current during the test run increased during the run from 20 to 80 nA as we reduced backgrounds. The optimal conditions were found to be 0.5% radiator, 5% converter and 12.7 mm collimator. During the test we reversed the main CLAS torus polarity to compensate for the different acceptance of in-bending/out-bending tracks, and also reversed the chicane polarity to minimize the systematic errors from the magnetic fields. The data shown here include both polarities of both chicane and torus.

The data shown here are extremely preliminary. No detector calibrations have been performed and the tracking software has not been optimized for our running conditions.

We have analyzed the test run data for $e^\pm p$ elastic events where we select events either with two positive tracks for e^+p elastic or with one positive and one negative tracks for e^-p elastic. Since the data are completely uncalibrated, we assume that a track with a higher β value is for a lepton and the other track is for a proton. In order to eliminate background, we required the z -component of the lepton vertex be within the hydrogen target, $v_z > -14.0 \text{ cm}$, as shown in Fig. 24(a) and Fig. 25(a) for lepton ϕ angle vs. v_z .

Since the initial lepton energy is unknown, it should be calculated. If an event is from $e^\pm p$

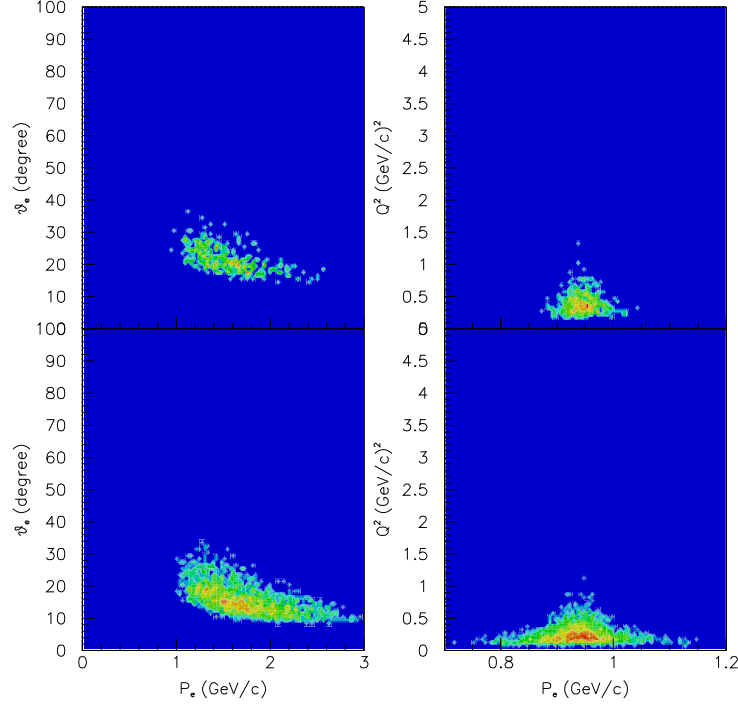


FIG. 23: e^\pm scattering angle (left) and Q^2 (right) vs. momentum after cutting on θ_X . Top and bottom plots are for e^+ and e^- respectively. Data from g11.

elastic scattering, the value of the initial lepton energy can be determined from the scattering angles θ_{e^\pm} and θ_p :

$$E_{beam} = m_p \left(\cot \frac{\theta_{e^\pm}}{2} \cot \theta_p - 1 \right)$$

or from the total event momentum along the z-direction:

$$E_{beam} = p_{e^\pm} \cos \theta_{e^\pm} + p_p \cos \theta_p$$

Fig. 24(b) and Fig. 25(b) show the calculated initial lepton energy difference (ΔE) between the two methods. We select events with $-0.2 < \Delta E < 0.3$ GeV. To complete the use of momentum conservation, we select events with the angle of the two-track total momentum relative to the z-direction, $\theta < 5^\circ$, as shown in Fig. 24(c) and Fig. 25(c). Fig. 24(d) and Fig. 25(d) show the difference between the lepton and proton ϕ angles, $\Delta\phi = \phi_{e^\pm} - \phi_p$: a black curve for all events, and a red curve after applying all three cuts. We can see that the remaining events form a nice peak at 180° , as expected for the $e^\pm p$ elastic events. Fig. 24(e) and Fig. 25(e) show the invariant mass W spectrum once good $e^\pm p$ elastic events are selected. The peak position for both channels is 0.946 GeV. This mass shift is typical of uncalibrated CLAS data. The results are very promising since the initial lepton energies are calculated from the reconstructed tracks event by event.

Fig. 24(f) and Fig. 25(f) show Q^2 vs. epsilon (ϵ) distributions for good $e^\pm p$ elastic events. The difference in yield for the two channels is due to different amounts of data taken with the two torus polarities. Note the large ϵ coverage, from 0.2 to 0.9. As expected, most of the events are at low Q^2 and large ϵ .

Even though data is completely uncalibrated, this demonstrates that we can clearly identify $e^\pm p$ elastic events. Calibrating the data will dramatically improve the timing, momentum and angle resolution, allowing much better and cleaner event identification.

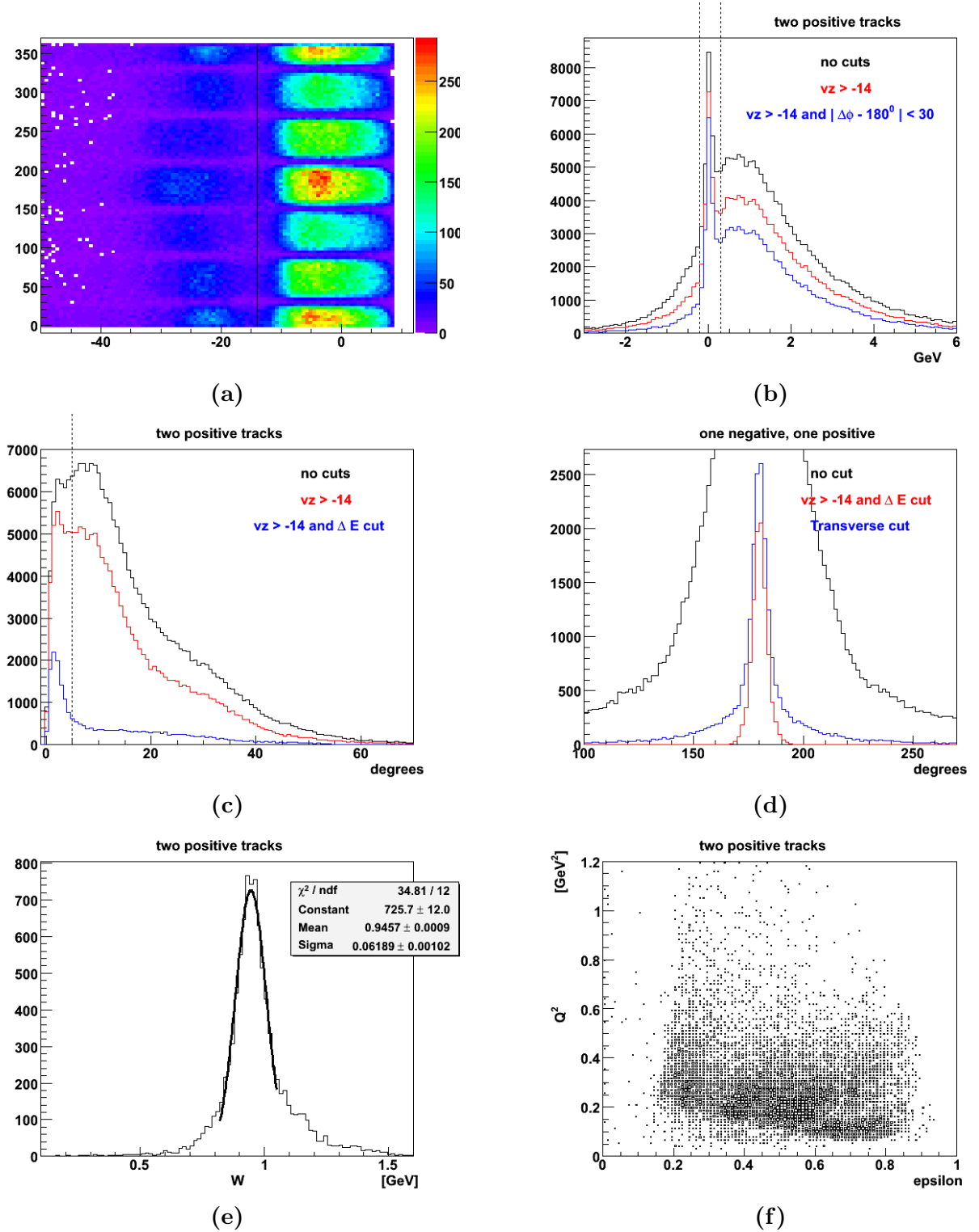


FIG. 24: Events with two positive tracks: (a) Positron ϕ angle vs. vertex z component (v_z). (b) Difference between the beam energies calculated from the positron and proton momenta, and from the positron and proton angles. (c) Angle of total momentum with the beamline in degrees. (d) The difference between the positron and proton ϕ angles. (e) Invariant mass W of the e^+p elastic events after all cuts. (f) Q^2 vs. epsilon distribution for e^+p elastic events. Uncalibrated test run data.

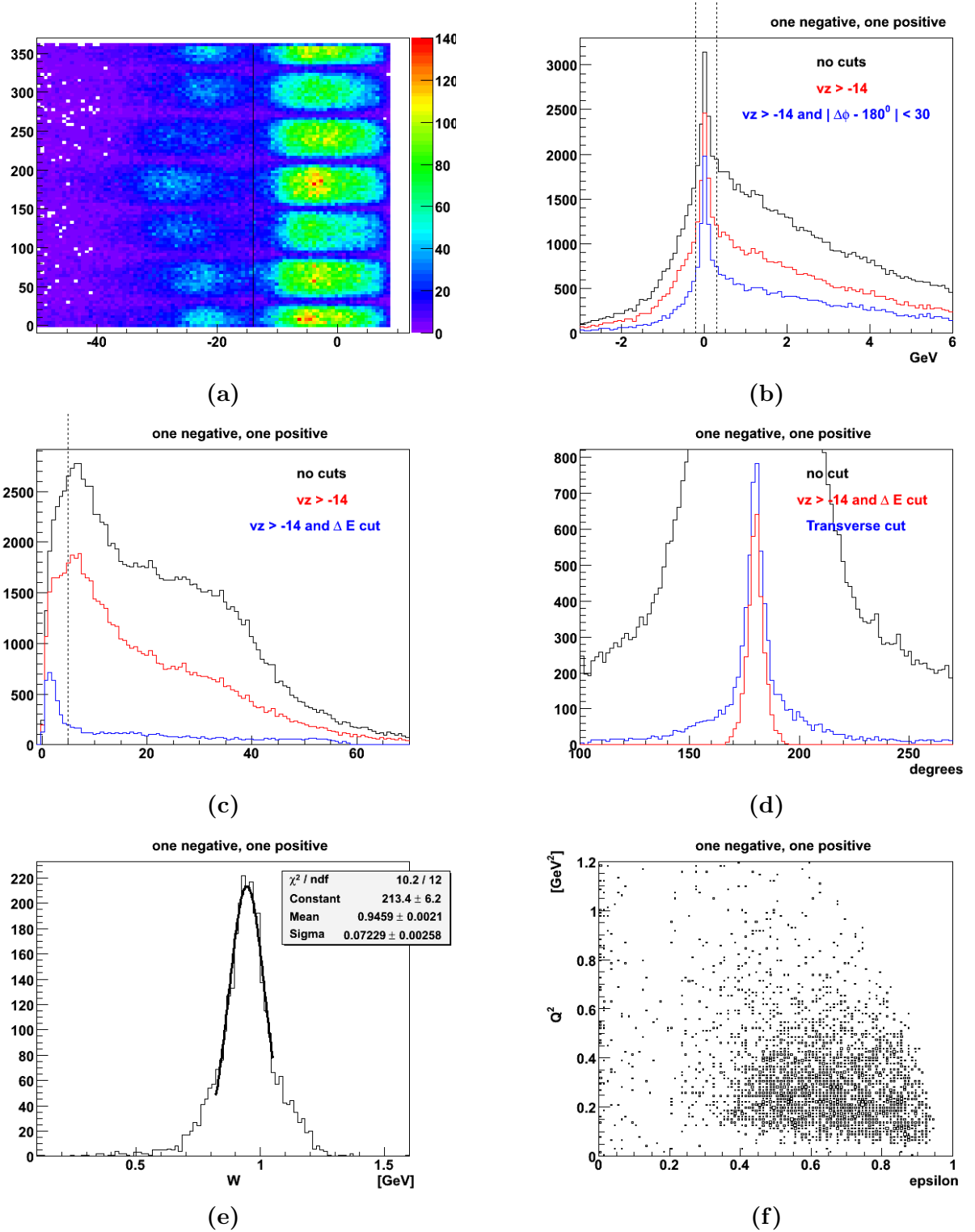


FIG. 25: Events with one negative and one positive track: (a) Electron ϕ angle vs. vertex z -component (v_z). (b) Difference between the beam energies calculated from the electron and proton momenta, and from the electron and proton angles. (c) Angle of the total momentum with the beamline in degrees. (d) The difference between the electron and proton ϕ angles. (e) Invariant mass W of the e^-p elastic events after cuts. (f) Q^2 vs. ϵ distribution for e^-p elastic events. Uncalibrated test run data.

G. Backgrounds

The prospect of creating secondary beams always raises issues of backgrounds and beam quality. The technique proposed here for producing the lepton beam is relatively clean, partly because the experiment can be successfully performed with a small beam current, taking advantage of the large acceptance of CLAS. Nonetheless, because of the spectrometer’s innately “open” design, it is quite vulnerable to background generated anywhere upstream, and so a thorough study is required.

There are several major categories of backgrounds to consider:

1. electromagnetic background generated from the photon collimator and from the new beamline devices: photon blocker, low-energy collimators, and the magnet yokes.
2. hadronic background from the photon blocker.
3. background from the tagger vacuum box and beam dump
4. Møller and Bhabha electrons produced in the hydrogen target.

These will be discussed in detail in the following sections.

Four different simulations have been employed for these studies, all based on GEANT. The first was a simulation of the beamline components that was based on GEANT 3.21. It contained the following elements: tagger magnetic field, sweeping magnet magnetic field, four dipole magnet magnetic fields; radiator material, converter material, four dipole magnet yokes, photon blocker, low-energy collimators, lead shield wall, shielding snout. No fringe fields were included. Subsequently this simulation was replaced by a much more detailed GEANT4 simulation that also contained a thorough treatment of the tagger vacuum box and many other shielding and beam transport components. The GEANT4 simulation was later updated to reflect the actual three-dipole chicane and new shielding components. Drawings of these components can be seen in Figures 5 and 6.

A specialized simulation was performed by using a GEANT 3 implementation [37],[38] referred to as the GDINR simulation[41]. It includes the radiator, photon collimator, converter, and the tungsten blocker, with no magnetic fields. This code is especially accurate for photo-producing hadrons. Because there are no magnetic fields, this simulation collides the produced lepton beam with the blocker, unlike the real situation; however, it is only a small error since the converter is quite thin. Thus it will give a slight overestimate of the background rates.

A fourth simulation was the standard CLAS simulation, referred to as GSIM [39]. It includes all components of CLAS and has been extensively tested and developed.

1. *Electromagnetic background from beamline components*

The luminosity during the October 2006 engineering run was limited by the Region 1 (R1) drift chamber occupancy. The results of measurements and configuration changes made during the engineering run suggest that the majority of the Region 1 occupancy was due to electromagnetic background from unnecessary material along the beamline. Simulation efforts subsequent to the engineering run have reproduced the general features seen during the test run.

The initial test run configuration differed from the setup shown in Fig. 26 in several ways: the collimator upstream of the lead (“RadPhi”) shielding wall had a 3 cm diameter, there was no cleanup collimator downstream of the RadPhi wall, and there was no concrete shield wall on the insertion cart. These were all added during the course of the run, as part of the effort

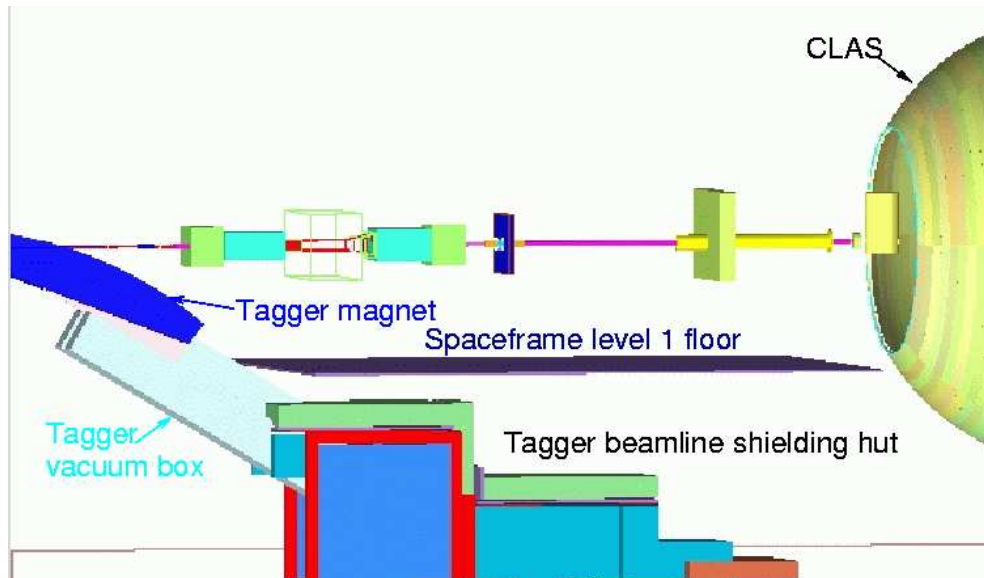


FIG. 26: Beamline and shielding configuration at the end of the October 2006 test run.

to reduce R1 occupancy. With the initial configuration, it was observed that switching off the power to the Frascati and Pair Spectrometer dipoles while leaving the beam current, converter and radiator fixed decreased the R1 occupancy by a factor of approximately 100. Thus, no more than 1% of the R1 occupancy was due to background from the photon blocker, tagger or tagger dump.

The vertex position determined by the fast online reconstruction showed a large number of tracks originating upstream of the target, as seen in the left panel of Fig. 27. The 3 cm diameter collimator just upstream of the RadPhi wall was replaced with a collimator 2 cm in diameter, which removed a substantial portion of the upstream background, as can be seen by comparing Fig. 27 left and right panels. The fast reconstruction routine is very inefficient at reconstructing tracks originating far from the target, so although the smaller upstream collimator produced a visually striking reduction in the reconstructed upstream background, its effect on the R1 occupancy was less dramatic.

The next modification to the beamline was stacking an array of concrete blocks (approximately 12" thick by 27" high by 42" wide) on the bottom of the torus cryoring. These blocks partially occluded the line of sight from the RadPhi wall aperture to S5 and S6 of the R1 drift chambers. This small shield reduced S5 and S6 occupancy in R1 by about 30%.

The last major configuration change to the beamline during the test run was the addition of a 36 mm X 36 mm cleanup collimator just downstream of the RadPhi wall, and the stacking of a 12" X 62" X 82" concrete wall on the insertion cart. Both of the modifications are shown in Fig. 26. Both of these modifications were performed during the same access, so their individual effects on R1 occupancy cannot be decoupled, but their collective effect was to reduce the R1 occupancy by a factor of approximately 2. After the cleanup collimator and insertion cart wall were added, a pile of lead bricks was stacked in front of the cleanup collimator, completely blocking the RadPhi wall aperture. With the RadPhi aperture blocked, the R1 occupancy decreased from approximately 2.5% to approximately 0.2% (with all other conditions held fixed). Blocking the aperture also decreased the trigger rate from 600 Hz to 200 Hz.

With all of the additional shielding elements in place, an empty target run reduced the R1 occupancy by 20% relative to the full target occupancy at the same current. This indicates that

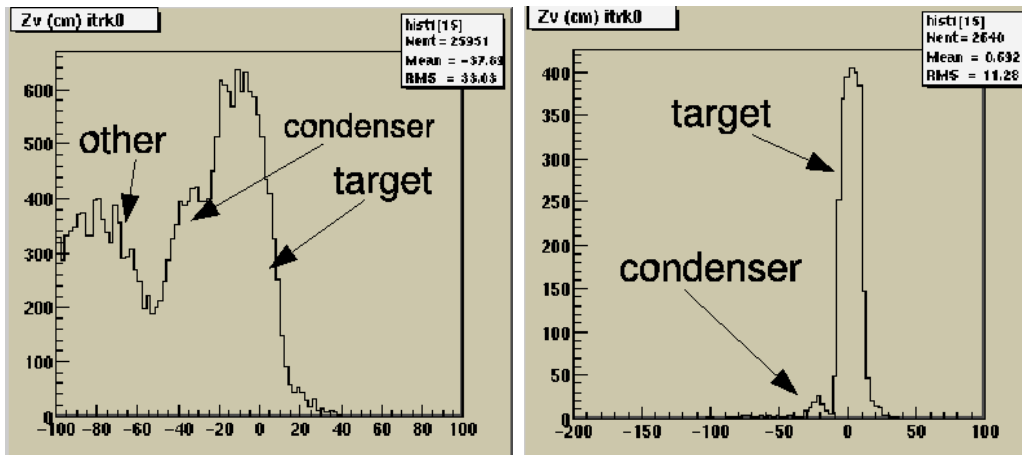


FIG. 27: z -vertex position of tracks reconstructed using the fast online tracking algorithm. The left figure is for 3 cm collimator used upstream of the RadPhi wall, while the right figure is for a 2 cm collimator.

there was still copious interactions between the lepton beams and the beamline environment. Improvements to the beamline, either by enhanced collimation or redesign of the cryotarget apparatus (increasing the diameter of the condenser ring and moving cryopiping farther away from the beamline) should be able to increase the luminosity by a factor of approximately six.

Because data on TOF rates was available from the 2005 test run, but Region 1 occupancies were not (the chicane was not used in the 2005 test run), the beamline simulation efforts prior to the 2006 engineering run focused on optimizing the lepton rate at the target relative to the TOF rate. Due to the factor of 20 improvements in the tagger-related backgrounds, Region 1 (R1) occupancy became the luminosity limiting factor. Several improvements to the simulation were subsequently made to improve its ability to estimate R1 occupancy. All of the test run shielding elements were added, as shown in Fig. 5. Additional cryo apparatus (cooler, cryotubing) were added to the simulation. All of the R1 wires were implemented in the simulation, as shown in Fig 28, giving the ability to simulate the effect of changing the beamline configuration on the R1 occupancy. The improved simulation has successfully reproduced the factor of two decrease in R1 occupancy that was obtained in the test run by adding the cleanup collimator and insertion cart wall. Additional collimation elements, shielding and cryo apparatus improvements will be extensively simulated and should result in a factor of six increase in the luminosity.

2. Hadronic background from the photon blocker

The hadronic rate from the photon blocker has been estimated using GDINR. While there will also be hadronic production from the nickel photon collimator and the low-energy collimators, the dominant rate that affects CLAS must be from the photon blocker, since it absorbs the full high-energy photon flux and it is only a few meters from the CLAS center. Typical rates are 10^6 Hz for pions, 10^7 for neutrons, and 10^6 for protons. These numbers partially take into consideration that the charged particles will lose energy in passing through the lead shielding wall as well as a significant length of the tungsten photon blocker and perhaps also iron magnet yokes. If these are scaled by π steradians, the resulting rates are 30 MHz for pions and protons, and 300 MHz for neutrons, spread out over the full volume of CLAS. The lower-energy component of the charged particles will not penetrate Region II because of the torus field, and

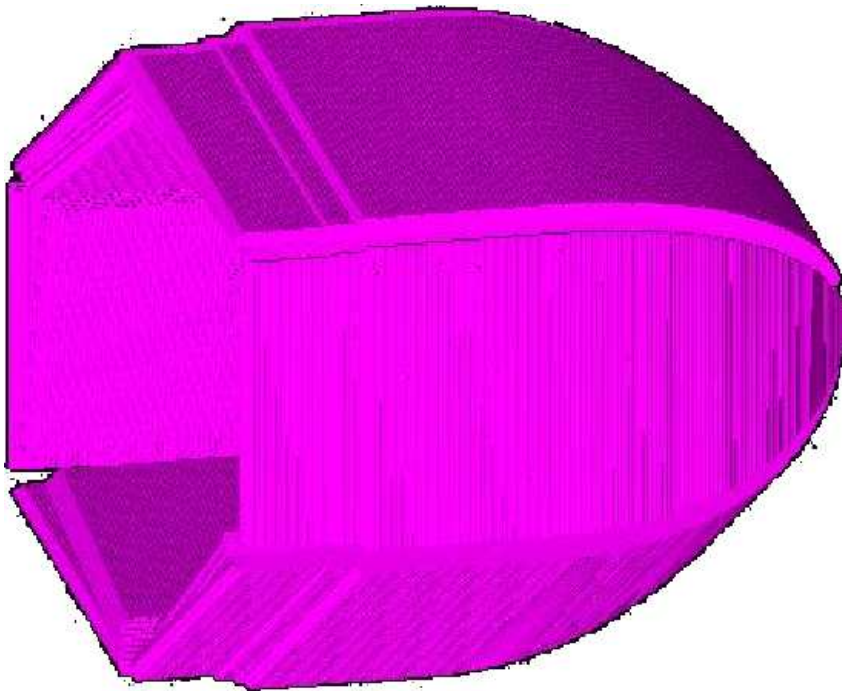


FIG. 28: GEANT4 simulation of R1 drift chamber wires. The rest of the beamline and detector elements have been removed for clarity.

any tracks going in the other regions will not point at the target. Although these rates are significant, they do not take into account the shielding effect of hadronic interactions in the magnet yokes nor the shield wall.

The evidence from the test run and from the GEANT4 simulations indicate that the hadronic background is much smaller than the electromagnetic background. Measurements of neutron flux using liquid scintillators (see next section for details) showed that the neutron rate was much smaller than the photon and charged particle rate. In addition, during the test run, we did not see drift chamber tracks pointing at the photon blocker, such as would be caused by pions or protons. Most importantly, when the chicane magnetic fields were off, so that all the photons and leptons were stopped by the photon blocker, backgrounds in the Region 1 drift chambers were very small.

3. *Tagger-related background*

The early test runs indicated that the backgrounds from the photon tagger and the tagger dump are much larger than those from the photon blocker. The first evidence of this was seen in the December test run when overall background rates in CLAS were observed to be independent of the presence of the photon blocker. We concluded that the background must be coming from the electron beam striking the exit flange of the tagger vacuum box. This comes from electrons that radiate photons with between 0.5 and 2% of the initial energy. Electrons that do not radiate leave the tagger vacuum box through the exit beam pipe. Electrons that radiate lower energy photons are bent a little more by the tagger and strike the exit beam pipe, a flange, or the end of the vacuum box itself (see Fig. 29).

In order to test this, we varied the tagger magnetic field (see Fig. 30) causing the electron



FIG. 29: The exit of the tagger vacuum box before modification. The tagger vacuum box is to the left and the beam exit pipe is the straight pipe exiting the figure in the middle of the right side. Note the small-diameter beam pipe, flanges, pump out port, etc.

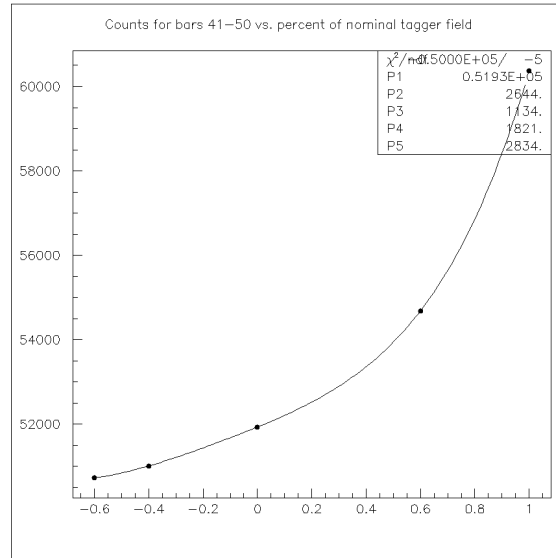


FIG. 30: Counts in back angle TOF detectors 41-48 vs shift in tagger magnetic field (%).

beam to sweep over the exit pipe and flange. When we decrease the tagger field, the electrons bend less and fewer electrons hit the bottom side of the beam pipe. When we increase the tagger field, the electrons bend more and more electrons hit the bottom side of the beam pipe. This shows that the material at the exit of the tagger is a significant source of CLAS background. We also observed that the rates seen by the CLAS TOF counters was largest in the rear lower portions, those closest to the tagger vacuum box exit.

The summer 2005 test run was designed to measure neutron backgrounds in the hall. We

0.5+ MeV Neutron background (g8)

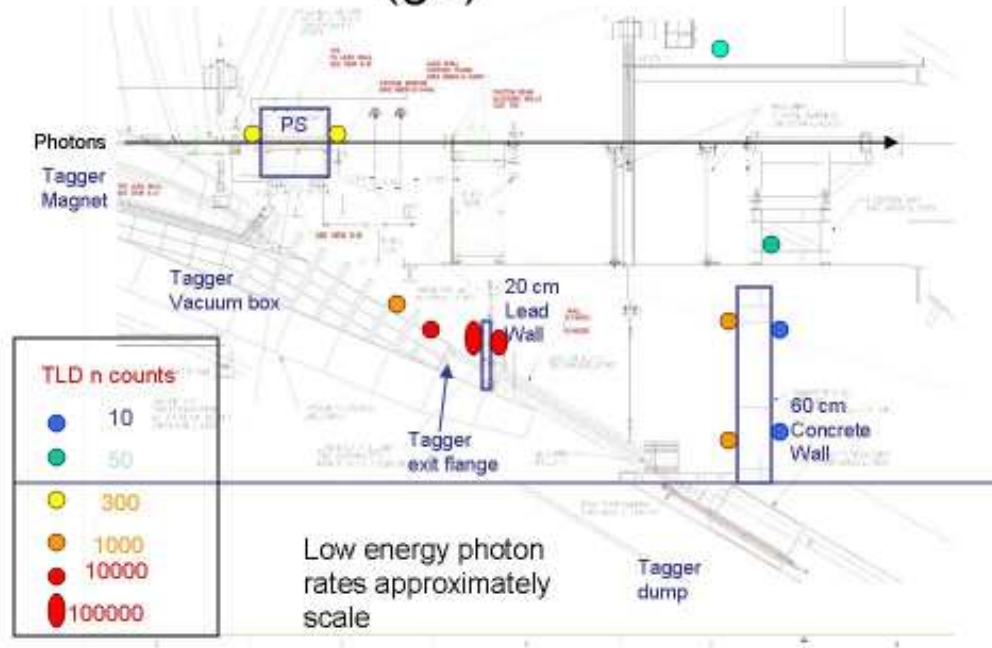


FIG. 31: This shows the relative counts in the CR-39 neutron detectors (≈ 0.5 MeV threshold) located around the hall during the g8 run. The tagger vacuum box exit shows the highest backgrounds and immediately downstream of the concrete shield wall shows the lowest backgrounds.

added a 60 cm thick, 120 cm wide, ≈ 3.5 m tall stack of borated polyethylene (BPE) shielding immediately downstream of the concrete wall on the floor of the hall. The BPE was placed on the beam-right side (so we could see if there was a difference between the unshielded and shielded sides). We then placed two liquid scintillator neutron detectors (ND) 2.5 m above the floor downstream of the concrete wall, one mounted beam right adjacent to the BPE shielding and one mounted beam left adjacent to the concrete wall. We placed two more ND on space frame level three, one inside a BPE “cave” and one on a floor of lead-bricks. We also placed about 20 TLDs with a special neutron-sensitive chip (CR-39) with a 0.5 MeV threshold in many locations about the hall. Since these tests were performed parasitically during the g8 run, they were done with a standard photon beam (and no photon blocker).

We recorded the prompt and delayed signals from the liquid scintillator neutron detectors in order to separate neutrons and non-neutrons. We found that very little of the background (1–3%) is actually neutrons. The BPE shield wall made little difference. There was no difference in the CLAS rates between sector 6 (beam left) and sector 5 (beam right). There was little difference between the radiation measured beam left and right by the CR-39.

The CR-39 measurements showed clearly that the tagger vacuum box exit generates a huge amount of neutron background and that much of this background is shielded from CLAS by the lead and concrete walls that existed downstream of the tagger at that time. Some of the neutron background comes from the photon beam line. Figure 31 shows the distribution of neutrons in the hall.

Guided by these results, we performed numerous simulations of various beamline and shielding configurations in an attempt to reduce the tagger-related background. Fig. 32 shows the

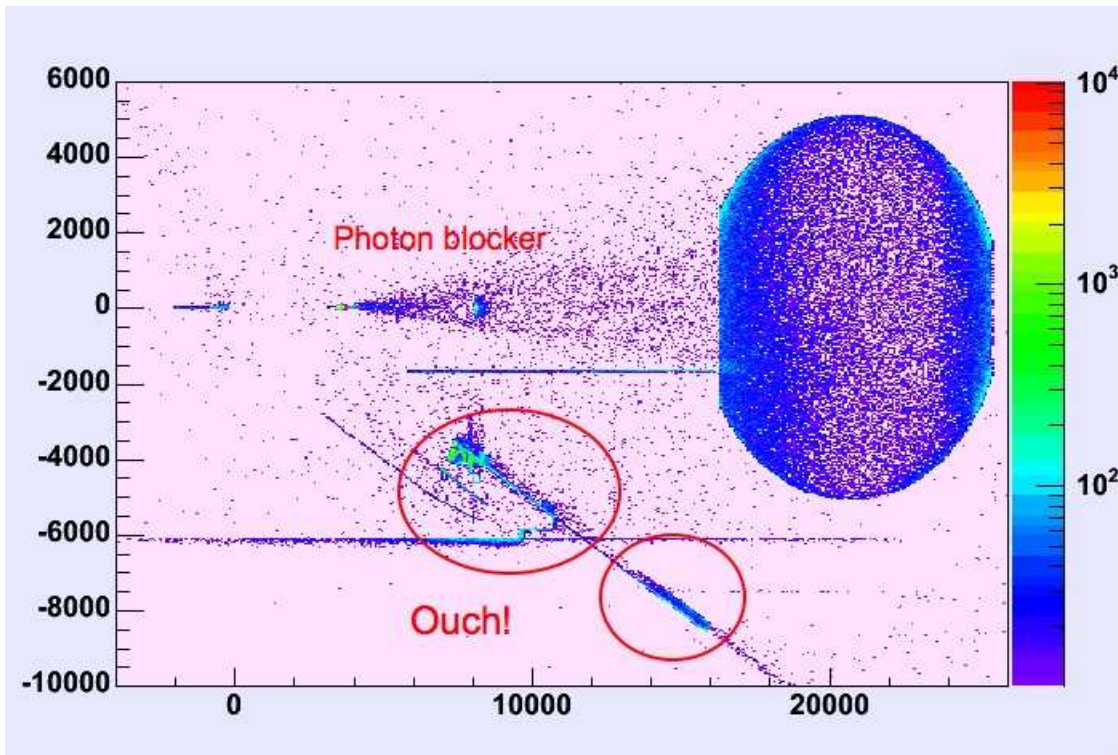


FIG. 32: Sources of the CLAS TOF background during the 2005 test run as simulated in GEANT4. Dimensions are in mm. The CLAS is the blue sphere on the right side of the figure. The beamline is at $y = 0$. The collimator and photon blocker show up along the beamline as bright spots at $x = 4000$ and 8000 . The floor of the hall is at $y = -6000$. The major source of background is the tagger exit beamline and beam dump (shown circled in red).

source of background in the CLAS TOF counters for our 2005 test run according to our GEANT4 simulations. The major source of background is the region of the tagger vacuum box exit. Closer examination showed that there was a huge amount of unnecessary mass in that region (see Fig. 29). Our simulations showed that replacing the exit flange with a larger aperture flange and the beam pipe with a large diameter helium bag would significantly reduce the background. Fig. 33 shows the result of the modifications. We also designed a much more robust shielding configuration (as shown in Fig. 26). These changes were made prior to the October 2006 test run.

The results of the October test run indicate that we reduced the tagger-related background by a factor of approximately 20. This background is still a factor, since the Region 3 occupancies in sectors 5 and 6 (the two sectors closest to the tagger exit beam line) are 50 to 100% higher than sectors 1–4. We measured background rates in several locations in and around the tagger exit line and dump shielding. These measurements plus additional simulation will lead to yet better shielding and a further reduction in this background.

4. Møller/Bhabha electrons

$0.5\mu\text{A}$ of beam current on a 1% radiator and 5% convertor will produce about 120 pA of total current (60 pA each of e^\pm) on the 40-cm liquid hydrogen target. This corresponds to a



FIG. 33: The exit of the tagger vacuum box after modification. The vacuum window is where the pump out port and beam pipe previously attached. The beam pipe has been replaced by a helium bag. Note the absence of pipes, flanges, and other material.

luminosity of $1.3 \times 10^{33} \text{cm}^{-2} \text{s}^{-1}$. This is higher than CLAS can normally run without using the minitorus. Use of the existing minitorus is not optimal, because the downstream aperture through the magnet is smaller than the lepton beam that needs to pass through it. Two clear possibilities exist for managing this background: construct a new minitorus, or add passive shielding in front of the Region 1 drift chamber.

In the engineering run, two devices were used for Møller suppression. The first was a conical lead shielding “bullet” mounted 14” downstream of the target cell. The aperture of the bullet was large enough to intercept particles exiting the target cell at polar angles of 15° or less. The second was a cylindrical plastic shield which fit over the scattering chamber. The plastic shield was constructed so that half (covering particles scattering into three of six CLAS sectors) had a thickness of 0.8 cm (approximately 1g/cm^2) and the other half had a thickness of 1.2 cm. The target cell, plastic shield and shield bullet are illustrated in Fig 34. The intention of using the two different thicknesses was to compare the effect on rates and angular resolution of varying the shield thickness.

The plastic shield was removed early in the engineering run. At the time it was removed, the R1 occupancy was dominated by backgrounds generated upstream of the target area, so any effect that the shield had was not visible. Later in the engineering run a large concrete-block shielding wall was stacked on the insertion cart, making it impossible to retract the target and reattach the plastic shield.

The plastic shield and lead bullet were added to the GEANT4 simulation of the target area. Fig. 35 shows the effect of the shielding bullet and various thicknesses of plastic shield on the energy spectrum of electrons that intersect R1 of the drift chambers. The multiple scattering of protons passing through the (thinner side) of the plastic shield used for the test run is estimated to be 4.7 mr for 800 MeV/c protons. The intrinsic azimuthal angle resolution of CLAS is 8 mr (sigma), which would be increased to 9.3 mr by the addition of the plastic shield.

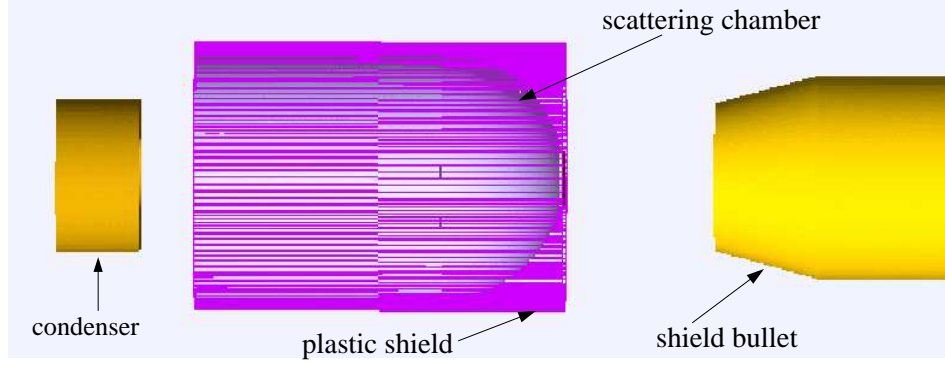


FIG. 34: GEANT4 implementation of condenser, scattering chamber, plastic shield and lead shielding bullet. Additional material in the target area has been removed for clarity.

If necessary, a new minitorus can be constructed that has a larger downstream aperture; operational experience with ‘straight-track’ runs taken for aligning drift chambers indicate that only one-third of the standard mini-torus field would be needed to run this experiment[42]. Therefore, the perturbation on the charged particle tracks would be quite small. While in principle there will be outgoing positrons from Bhabha scattering which will be anti-shielded by a minitorus, the rate of these is greatly suppressed relative to scattered electrons.

It is not yet clear which of these two alternatives is preferable, however, both are feasible.

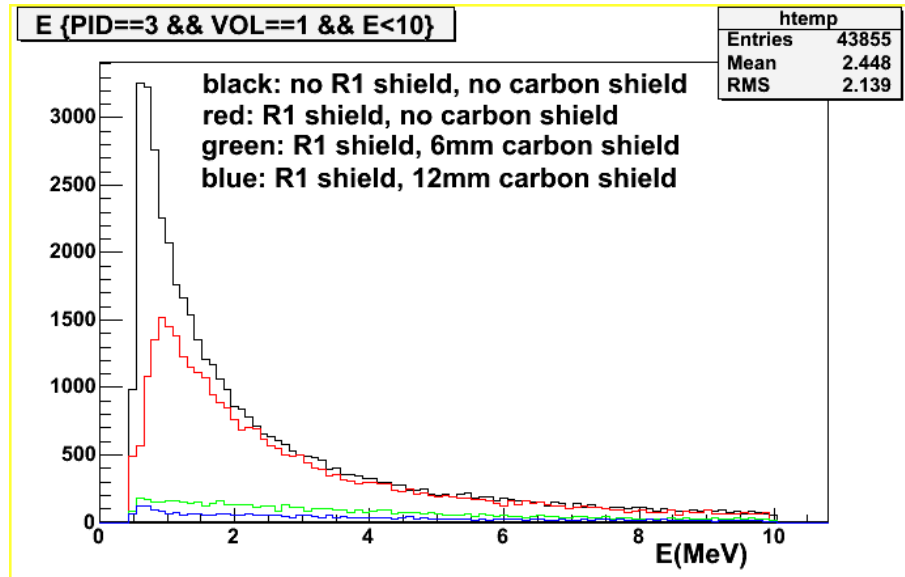


FIG. 35: Results of a GEANT4 simulation of the effect of the lead shielding bullet and plastic shield on the low-energy electrons entering Region 1.

H. Experimental Luminosity

The primary problem with a tertiary beam is achieving sufficient luminosity to perform the measurement. The 2004 proposal claimed that we could create lepton beams of a few hundred picoAmperes each and achieve physically meaningful results up to $Q^2 = 2 \text{ GeV}^2$ over the entire range of ε . The October 2006 test run showed that we know how to achieve at least 24% of that luminosity. We expect that we can gain another factor of 4 through further simulation and shielding.

The total luminosity is the product of beam current, radiator thickness, convertor thickness, and target thickness, with a correction factor for beam removed by collimators. The 2 mm collimator used in the original proposal removed about half of the photon beam. The 12.7 mm collimator used in the test run removed very little of the photon beam and thus increased the effective luminosity (relative to the PAC 26 proposal) by a factor of two. This factor is included in the relative luminosities of Table I.

TABLE I: Proposed, achieved, and achievable luminosities. ‘PAC 26’ refers to the proposed luminosity in the 2004 proposal; ‘Test Run’ refers to the luminosities achieved in the Oct 2006 test run; ‘Widen cryo-apertures’ refers to the luminosities achievable if we rebuild the cryotarget to increase the apertures of the heat exchanger and condenser; ‘further sims’ refers to the expected gains from increased shielding based on further simulation.

| Item | PAC 26 proposed | Test Run achieved | Widen cryo- apertures | further sims and shielding |
|---|--------------------|----------------------|--------------------------|-------------------------------|
| Primary electron beam energy (GeV) | 5.7 | 3.3 | 5.7 | 5.7 |
| Primary electron beam current (μA) | 1.0 | 0.08 | 0.24 | 0.5 |
| Radiator thickness ($\%X_o$) | 5 | 0.5 | 0.5 | 1.0 |
| Photon collimator aperture (mm) | 2 | 12.7 | 12.7 | 12.7 |
| Converter thickness ($\%X_o$) | 2 | 5 | 5 | 5 |
| Cryogenic hydrogen target length (cm) | 20 | 20 | 40 | 40 |
| Luminosity (fraction of PAC 26 proposal) | 1 | 0.04 | 0.24 | 1 |

There are generally two limitations. The Region 1 drift chambers are sensitive to the quality and quantity of the lepton beams exiting the post-chicane collimator and to the placement of material in and around the beam line. The Region 3 drift chambers are sensitive to background coming from the photon and tagger beam lines. The rate in Region 3 is proportional to the photon flux (ie: to primary beam current times radiator thickness). We have already reduced this rate by a factor of about 20 with the new beam line and shielding configuration. We expect that this rate can be further reduced by a factor of 4 through further simulation and shielding.

The maximum luminosity achieved in the test run was about 4% of that proposed in 2004 to PAC 26 (columns 2 and 3 of Table I). As discussed previously, the primary limitation was background in the Region 1 drift chambers from leptons scattering from cryotarget heat exchangers. We can eliminate this by rebuilding the heat exchanger to have a much larger aperture. This would allow us to increase the luminosity by a factor of six.

If we widen the cryo-apertures with the existing shielding configuration, we can increase the photon flux by a factor of three by either increasing the beam current or the radiator thickness (within the limitations of the Region 3 drift chamber occupancies). We can then increase the target length by a factor of two to achieve the overall factor of six increase.

This will allow us to achieve 24% of the proposed luminosity. During the October 2006 test run we have already decreased the background by a factor of 20 and we have identified several possible sources of remaining background. These include the concrete side walls of the tagger shielding bunker, the ‘tunnel’ shielding between the chicane magnets, the photon collimator, and the shielding and collimation following the chicane. We are confident that we can reduce the background by another factor of four through extensive simulation and shielding.

I. Systematic errors

The purpose of the experiment is to precisely compare the e^+p differential cross section to the e^-p differential cross section. Here is a list of the potential sources of systematic error:

1. differences in the positron and electron incident flux
 - differential electron-positron attenuation in matter
 - differences between low-flux and high-flux beams
 - differential trajectories through the magnetic system
 - imperfections in one pole face
 - changes in angle/position of the incident photon beam
 - reproducibility of magnetic field when switching dipole magnet polarities
 - magnetization of local objects
 - Earth’s magnetic field
2. differences in the acceptance of the protons from the two reactions
3. differences in the determination of the electron and positron momentum vector
4. differences in the acceptance of the electrons and positrons
 - CLAS geometrical acceptance differences
 - differential e^+/e^- attenuation (can also be caused by path length differences)
 - CLAS detector inefficiencies, errors and mis-calibrations
 - differential phi-focusing for trajectories near the torus coils
5. contamination by background process
 - inelastic lepton-proton scattering: $e^\pm p \rightarrow e^\pm p \pi$
 - virtual bremsstrahlung in the target: $\gamma p \rightarrow p \pi X$
 - virtual bremsstrahlung in the target walls: $\gamma n \rightarrow p \pi^-$

We will use several powerful techniques to reduce the effects of the systematic errors:

1. measure the flux of both incident beams, both destructively at the target and non-destructively where the beams are dispersed
2. use the same target for both beams
3. reverse the magnetic field in the separator magnet chicane, interchanging the paths of the two lepton beams

4. trigger on any two charged particles in opposite sectors (to avoid hardware electron/positron identification biases)
5. determine the scattering kinematics using only the proton information (independent of beam charge) and use the lepton only to determine that the event is elastic
6. use a low CLAS torus magnetic field
7. reverse the torus magnetic field, interchanging the scattered electron and positron trajectories
8. compare asymmetries measured in different CLAS sectors
9. reduce endcap contamination by cuts and by empty target subtraction
10. use the CLAS EC and Cerenkov counters to measure the pion contamination at forward angles

To first order, the electron and positron beam fluxes should be completely identical. The two beams are created simultaneously by pair production in a photon converter. The only differences in the two beams could come from a) differential beam attenuation in the finite thickness of the converter, b) differences in beam transport from the converter to the target, and c) differential beam attenuation in the 20-cm long target. According to the PDG, at lepton energies above 500 MeV, attenuation of positrons and electrons is dominated by bremsstrahlung (which is identical for both particles). Positron annihilation and Bhabha (e^+) and Moller (e^-) scattering are all negligible. With a 5% converter, about 2.5% of the converted leptons will emit bremsstrahlung photons in the converter. However, positron and electron bremsstrahlung is identical. The cross section for Compton scattering in the converter is more than 100 times less than pair production for 500 MeV photons (and drops rapidly with photon energy). Similarly, the 20 cm LH_2 target is about 3% of a radiation length so differential attenuation in the target is less than 0.1%. Therefore differences in beam flux should only come from differences in beam transport. We will deal with these possible differences in two ways.

We will significantly reduce any effects from asymmetric beam transport by reversing the magnetic fields in the separator magnet chicane. This will interchange the incident electron and positron beams. We will carefully cycle the chicane magnets to minimize the effects of hysteresis. To the extent that the field values are reproducible, and that there are no other magnetic fields affecting their trajectories, the electrons and positrons will follow exactly the same path when the separator field is reversed. We will measure the individual beam positions as a function of chicane current whenever we reverse the chicane field. Averaging the data taken with the two separator field polarities will average out any differences in the beam transport through the chicane and any differences in the flux monitoring detectors.

There will be some unavoidable difference in the magnetic fields of the two chicane polarities due to magnetization of nearby materials, non-reproducibility of the magnetic field, and the Earth's magnetic field. This difference will have two possible effects. The first would be to change the amount of flux reaching the target and the second would be to change its position on the target.

We expect that the difference in $\int B \cdot dl$ between the path followed by electrons and that followed by protons with reversed chicane field (and vice versa) will differ by at most 1%. Since all of the beam, except that part cut off by the low-energy collimators, is transported to the target, a small change in the magnetic transport will only affect the value of the low-energy

cutoff. Since the software threshold on the incident particle energy will be larger than the collimator-cutoff, a small shift in the collimator cutoff will not affect the incident flux.

Non-reproducibility and non-reversibility of the chicane magnetic fields will change the beam position on target by about 1 mm. The maximum beam deflection for low energy ($E = 0.5$ GeV) leptons in the chicane is 20 cm. A 1% difference in $\int B \cdot dl$ would then shift the path of the low energy leptons by 2 mm. We will measure the position and energy distribution of each lepton beam after each field reversal in the chicane to an average of better than 1 mm.

Since over 99% of the incident leptons will hit the 10-cm diameter target and since the lepton distribution is strongly peaked at the center of the target, a 1 mm shift in the beam centroid will change the low energy part of the beam that hits the target by less than 0.1%. The offset of higher energy leptons would be significantly smaller as it is proportional to $1/E$.

The variation of beam position on target will affect the average target length. The 20-cm long, 10-cm diameter target will not be a perfect cylinder. The downstream target face will have a radius of curvature of probably 20 cm. This means that it will be 207 mm long in the center and 200 mm long at the edges. A 1-mm beam shift will change the average target thickness (for that energy lepton) by at most 0.2%. In addition, we will apply software cuts to remove the effects of the entrance and exit windows. This will also remove the effects of the downstream window bulge. If necessary, we can also use a pressurized gas capsule to force the upstream window to bulge in, canceling the effects of the downstream bulge and making the target length constant.

The geometrical acceptance of CLAS is determined primarily by the torus cryostat. The cryostat is 1.5 m from the target. A 1 mm shift in beam location will thus decrease the solid angle in one sector by approximately 0.1% and increase it in the opposite sector by the same amount.

We will measure the centroids of each of the lepton beams as a function of incident lepton energy. We will easily be able to measure centroid locations to within 1 mm with the proposed flux monitoring system.

We will also directly measure the flux in the two beams for both chicane polarities. The flux measurement serves two purposes. It will measure whether the e^+ and e^- beams are identical and, if they are not identical, how much they differ as a function of energy and position. It will also measure the absolute energy distributions of the two beams.

The flux measurement techniques are described in detail in Sec IV D. We will measure the flux of each beam immediately in front of the target as a function of energy and position on target using a position sensitive detector followed by an electromagnetic calorimeter. We will also measure the flux of the unused low-energy part of each beam immediately before the second chicane magnet where the beams are separated and dispersed.

We will make two sets of flux measurements. At very low rate we will block one lepton beam and measure the flux of the other beam using the calorimeter at the target. Comparing the beam fluxes measured by the calorimeter for the two beams will tell us whether they are identical at the target (and by how much they differ if they are not identical). At a rate of 1 kHz (to minimize all dead times), we can acquire enough statistics on the beam distributions in under an hour. This will allow us to compare the beam fluxes to much better than 1%.

At the same time that we measure the flux using the calorimeter, we will measure part of the unused low-energy part of the beams in the dispersed region. By using both the dispersed detector and the calorimeter, we can cross-calibrate the two detectors. At normal rates, we cannot use the calorimeter so we will use the dispersed detectors to continuously monitor the two fluxes. This will tell us how the relative rates in the two beams scale when we increase the beam flux.

The electron and positron beams will be simultaneously incident on the same target. Thus, the CLAS proton acceptance will be the same for both reactions. Similarly, the proton momentum determination will be the same for both reactions.

We will trigger on two charged particles in opposite CLAS sectors. We will then use the e^\pm angle and the proton kinematics to define the reaction (including determining the incident lepton energy), with only loose cuts on the e^\pm momentum to identify elastic scattering reactions. (Note that the measurement of the angles of the outgoing leptons are determined primarily by the Region I drift chambers where there is no magnetic field. There should thus be little difference in the measurement of the electron and positron angles.) In this way, differences in the measurement of the electron and positron momentum vectors will have a minimal effect. Because the kinematics are overdetermined, there are several cross-checks that can be used to study this.

The largest source of experimental uncertainty is the different acceptance for electrons and for positrons. The first method of reducing these effects is to not trigger on a lepton (i.e.: to not require the Cerenkov counter or the electromagnetic calorimeter in the CLAS trigger). There are two remaining sources of acceptance differences: a) missing or inefficient detector channels and b) the CLAS geometry. The effects of missing or inefficient detector channels can be modeled using the CLAS Monte Carlo software package GSIM and the results of that modeling can be tested by comparing the results from the six different sectors of CLAS. This will reduce the effects of bad channels to significantly less than the statistical uncertainties.

Electrons and positrons have different geometrical acceptance in CLAS because one bends inward (toward the beamline) and the other bends outward. We will reduce this effect by operating the CLAS at the lowest possible magnetic field where we can still readily distinguish between elastic and inelastic scattering.

The remaining effects of the geometrical acceptances on the lepton acceptance can also be minimized. In general, there are two cases: a) large lepton scattering angle (small ε) and b) small lepton scattering angle (large ε). We will treat these separately.

For large lepton scattering angle, the CLAS acceptance is large and slowly varying (see Fig. 38). The azimuthal (ϕ) acceptance in each sector is significantly greater than 67% (i.e.: $\Delta\phi > 40^\circ$ out of a possible 60° in each sector) for scattering angles $45^\circ < \theta < 130^\circ$. By making a tight cut on ϕ (e.g., $-20^\circ < \phi < 20^\circ$ in each sector), we can ensure that the electron and positron acceptances are identical. We also significantly reduce the affects of ϕ -focusing near the torus coils.

For small lepton scattering angles, the CLAS acceptance is small and rapidly varying. Therefore the electrons and positrons will have very different acceptances. We can compensate for this by reversing the CLAS torus field which, in effect, interchanges the scattered electron and positron trajectories. By averaging measurements with the two torus field polarities, we can completely account for the differences in the geometrical acceptance. However, we need to make sure when do this that the proton acceptances for the two torus field polarities are identical. Fortunately, when the leptons are at small angle, the proton will be detected at larger angles ($60^\circ < \theta_p < 90^\circ$) where the acceptance is larger and more slowly varying. By making a tight cut on ϕ_p (e.g., $-20^\circ < \phi_p < 20^\circ$ in each sector), we can ensure that the proton acceptances for the two field polarities are identical.

Differential e^\pm attenuation in the several meter flight path from the target through the detectors will also be negligible, since e^\pm at these energies is dominated by bremsstrahlung, which is identical for both particles.

There is a possibly significant target-related background from lepton virtual bremsstrahlung in the target resulting in $\gamma p \rightarrow p\pi^+\pi^-$ events where one of the pions is undetected. Most of these will be rejected by the same cuts that eliminate inelastic lepton scattering events $ep \rightarrow ep\pi^0$.

TABLE II: Anticipated systematic uncertainties. The error refers to the uncertainty in the e^+/e^- cross section ratio.

| Source | Error (%) |
|--|-----------|
| e^+/e^- flux differences | 0.2 |
| Proton acceptance differences | 0 |
| e^+/e^- momentum measurement | 0.1 |
| e^+/e^- geometrical acceptance differences | < 1 |
| e^+/e^- detector efficiency differences | 0.1 |
| inelastic contamination | 0.1 |
| Total | < 1 |

The remaining background will merely dilute the e^+p/e^-p cross section ratio unless there is a charge anisotropy in the pion angular distribution (e.g., positively charged pions are more forward scattered than negatively charged pions). We can measure the contamination of the forward angle elastic leptons by using the CLAS EC, Cerenkov and LAC detectors to identify pions and leptons.

We will completely eliminate the background from $\gamma n \rightarrow p\pi^-$ by a) cutting the target to eliminate the target wall region and b) measuring the empty target and subtracting it from the full target runs.

In summary, the residual errors are likely to be the following (see Table II):

- an incorrect assignment of Q^2 and E_0 due to systematic errors in the measurement of the proton kinematic variables. This will cancel in the ratio e^+p/e^-p .
- the effect of detector channels changing characteristics. This will be reduced to less than the statistical error by a combination of simulation and comparison among the six sectors.
- the ratio of the incident lepton fluxes will be calculated and simulated, and directly measured as part of the experiment.
- the effects of differential electron and positron acceptances will be minimized with geometrical cuts and by reversing the CLAS torus field.

In conclusion, the systematic errors can be controlled to better than 1% because of the uniquely symmetric nature of the interaction under study, in combination with the large angle and momentum acceptance of CLAS.

J. Rate estimate

The beam of positrons and electrons obtained from the apparatus has a wide range of energies. The rate estimate has been obtained by weighting the elastic scattering rate by the energy profile of the incident leptons and the CLAS acceptance. The lepton energy profile has been calculated using a detailed GEANT simulation of the entire beamline apparatus, starting with a 5.7 GeV electron beam incident on the tagger radiator.

Elastic scattering is fully characterized by two kinematic variables. Because two-photon exchange is optimally revealed by its dependence on the variable ε , and because of the interest

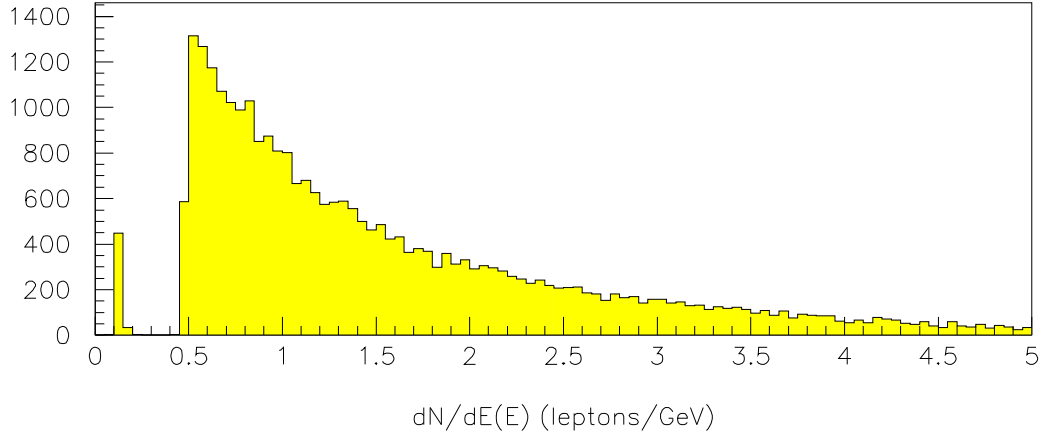


FIG. 36: The spectrum of lepton energies $\frac{d\mathcal{L}^{e^+e^-}}{dE}(E)$ incident on the cryotarget from a GEANT simulation. This yield corresponds to approximately 60 million electrons incident on the tagger radiator. The gap in energies seen in this figure is due to the low-energy collimators, which remove leptons that are too low in energy to contribute to the data of interest. The remaining very low energy leptons are a residual background.

in extending the impact of these measurements to those at higher Q^2 , a natural choice is to cast the problem in terms of these two variables.

In these variables, the double-differential counting rate is given by

$$\frac{d^2 R}{dQ^2 d\varepsilon} = \frac{d^2 R}{dE d\Omega} \cdot \frac{dE d\Omega}{dQ^2 d\varepsilon} = \frac{d}{dE} \left(\frac{dR}{d\Omega} \right) \cdot \frac{dE d\Omega}{dQ^2 d\varepsilon} \quad (6)$$

The rate per unit solid angle $\frac{dR}{d\Omega}$ is given by

$$\frac{dR}{d\Omega} = \int \frac{d\mathcal{L}^{e^+e^-}(E)}{dE} \cdot \frac{d\sigma}{d\Omega} dE \quad (7)$$

where $\frac{d\mathcal{L}^{e^+e^-}(E)}{dE}$ is the energy-dependent luminosity distribution of the leptons. This distribution, shown in Fig. 36, was derived from a GEANT simulation of the beamline. Substituting this expression for $\frac{dR}{d\Omega}$ into Eqn. 6 yields the final result:

$$\frac{d^2 R}{dQ^2 d\varepsilon} = \frac{d\mathcal{L}^{e^+e^-}(E)}{dE} \cdot \frac{d\sigma}{d\Omega} \cdot \frac{dE d\Omega}{dQ^2 d\varepsilon} \quad (8)$$

The rate calculation was performed numerically on a dense rectangular grid in Q^2 and ε to preserve accuracy; the final results were obtained by integrating these small bins into larger bins for data presentation. The number of counts N in a larger bin of $Q_1^2 < Q^2 < Q_2^2$ and $\varepsilon_1 < \varepsilon < \varepsilon_2$ is given by the time duration of the experiment multiplied by the rate $\frac{d^2 R}{dQ^2 d\varepsilon}$ and integrated over the larger bin limits:

$$\int_{Q_1^2}^{Q_2^2} \int_{\varepsilon_1}^{\varepsilon_2} \frac{d^2 N}{dQ^2 d\varepsilon} \cdot A(Q^2, \varepsilon) dQ^2 d\varepsilon \approx \sum_i \sum_j \frac{d^2 N}{dQ^2 d\varepsilon} \cdot A(Q^2, \varepsilon) \Delta Q_i^2 \Delta \varepsilon_j \quad (9)$$

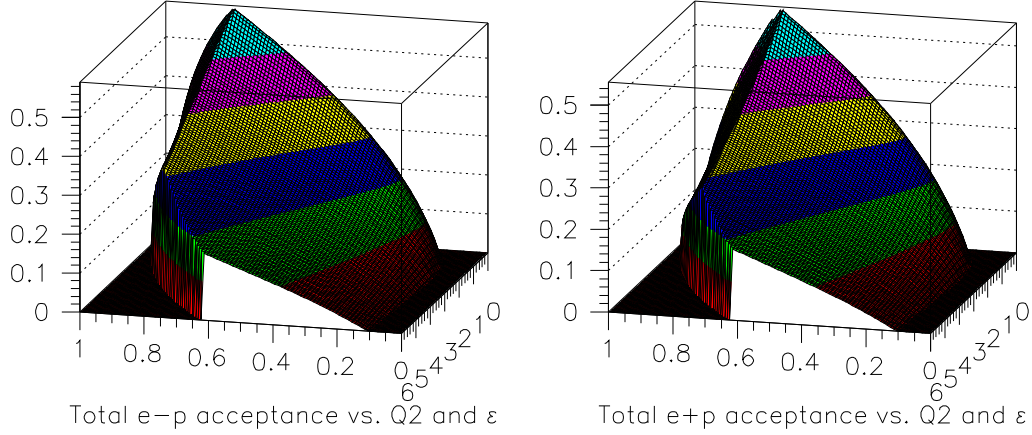


FIG. 37: Parameterized CLAS acceptances for elastic scattering events as a function of Q^2 and ϵ . Because the particles are completely correlated in this reaction, for each bin in $dQ^2 d\epsilon$ the single particle acceptance (shown in Fig. 38) was computed for both particles and the smaller acceptance was taken as the event acceptance. No other losses were accounted for in the calculation, such as detection and reconstruction inefficiencies.

where $A(Q^2, \epsilon)$ is the CLAS acceptance function shown in Fig. 37, which was derived from the single particle acceptance functions shown in Fig. 38. The RHS indicates the numerical integration procedure where i and j label the small bins in Q^2 and ϵ and $\frac{d^2 N}{dQ^2 d\epsilon}$ is an average value within the two-dimensional $Q^2 - \epsilon$ bin. The distribution of total counts as a function of Q^2 and epsilon is shown in Fig. 39. Leptons of less than 25° in scattering angle were removed, since systematic errors in the acceptance ratio are not as well controlled for these angles.

The statistical quality of the data predicted by this rate calculation is indicated in Fig. 40 in

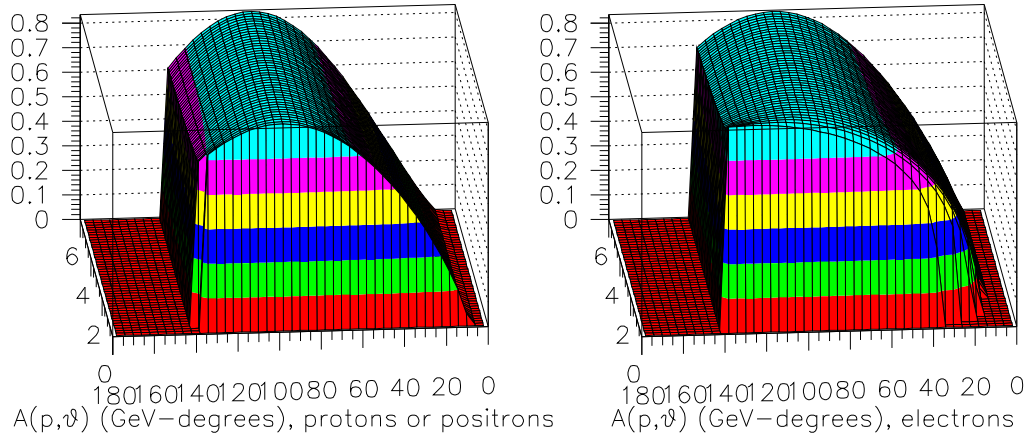


FIG. 38: Parameterized CLAS acceptances for single particles as a function of momentum and polar angle. This function takes into account the magnetic field value, the charge of the particle, and its momentum vector. Note that the acceptances are nearly identical for positrons and electrons over a broad kinematic range. This is an important feature of CLAS that helps to minimize systematic errors due to acceptance differences.

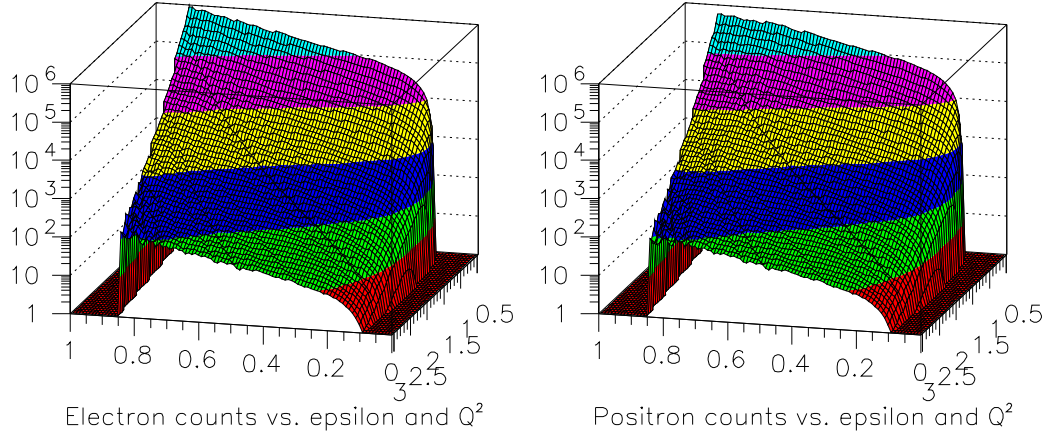


FIG. 39: The number of electron-proton and positron-proton scattering events as a function of Q^2 and ε from the rate calculation. Bins are 0.06 GeV^2 in Q^2 and 0.01 in ε .

one particular binning scheme. The Q^2 bins indicated are approximately the true bin centers, i.e. the Q^2 bins are asymmetric about the indicated values, and there are no gaps between the bins - all of the data is used. A band of $\pm 1\%$ is indicated on the figures for reference. The parameters used for the calculation are indicated in Table III.

TABLE III: Anticipated running conditions and beamtime request.

| Item | Value |
|---|-------------------|
| Primary electron beam energy | 5.7 GeV |
| Primary electron beam current | $0.5 \mu\text{A}$ |
| Radiator thickness | $1\%X_o$ |
| Converter thickness | $5\%X_o$ |
| Cryogenic hydrogen target length | 40 cm |
| Torus current | 1000 A |
| PAC days for data acquisition | 27 |
| Additional days for flux measurement and torus polarity changes | 3 |
| Additional days for commissioning of all devices | 5 |
| Total PAC days requested | 35 |

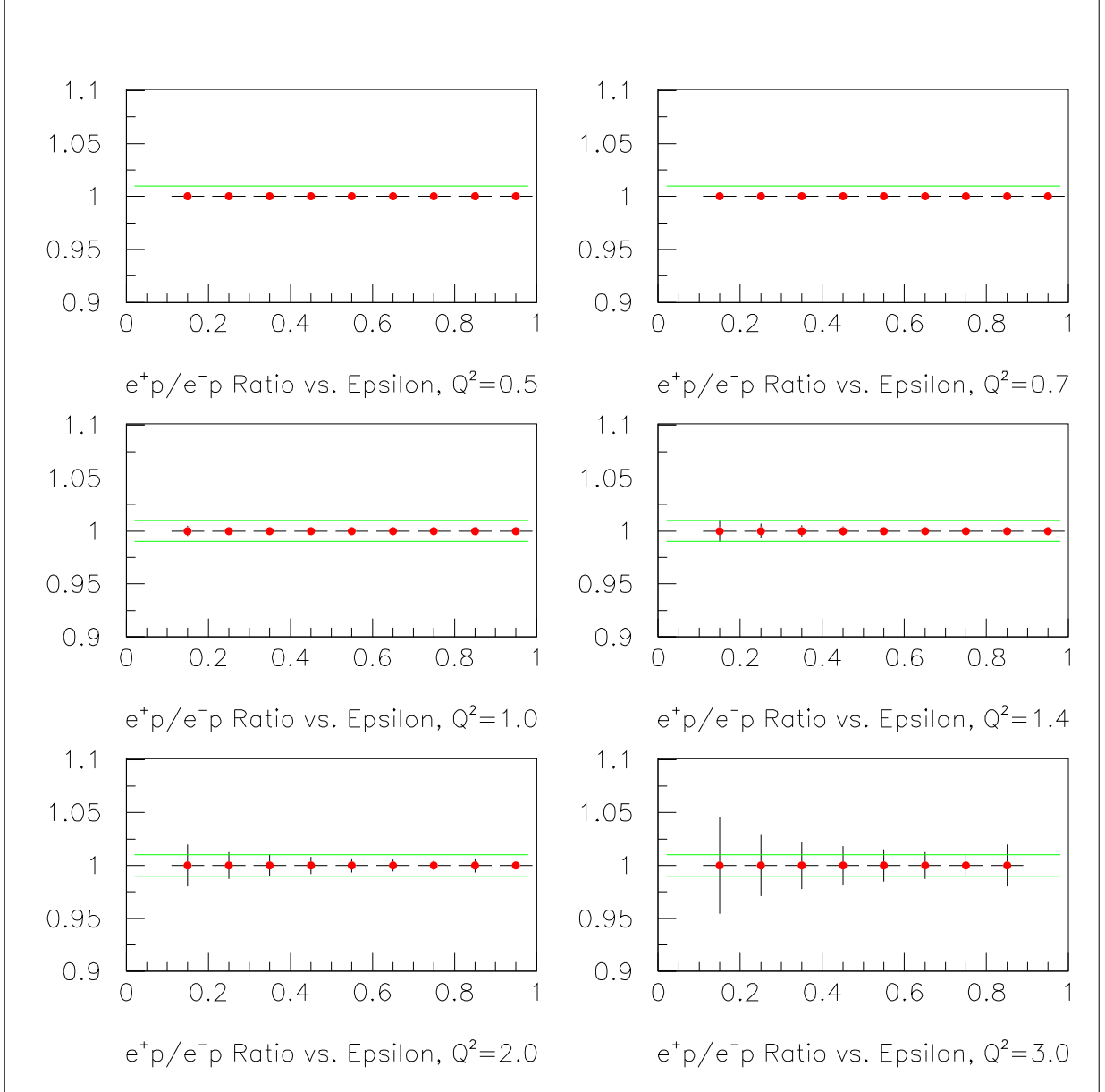


FIG. 40: Statistical errors in a particular binning scheme. The Q^2 values indicated in the captions are approximately true bin centers. A band of $\pm 1\%$ is indicated as a reference.

V. BEAM TIME REQUEST AND ANTICIPATED RESULTS

The running conditions and anticipated beam request are shown in Table III. The conditions selected are based on best known practices, GEANT simulation, and cryotarget technology that is known to be achievable. The limiting statistical error is for smallest epsilon. The total number of PAC days required is 35, which allows for 3 days of lepton flux measurements and several torus polarity changes, and 5 days for commissioning of the new devices (two flux detectors, magnet chicane, movable low-energy collimators, movable photon blocker, shielding configuration).

A plot of the expected data quality is shown in Fig. 40. This may be compared with the data of Fig. 3 which are shown on a much greater vertical axis range. A very significant improvement in our understanding of the epsilon dependence of this ratio would clearly be

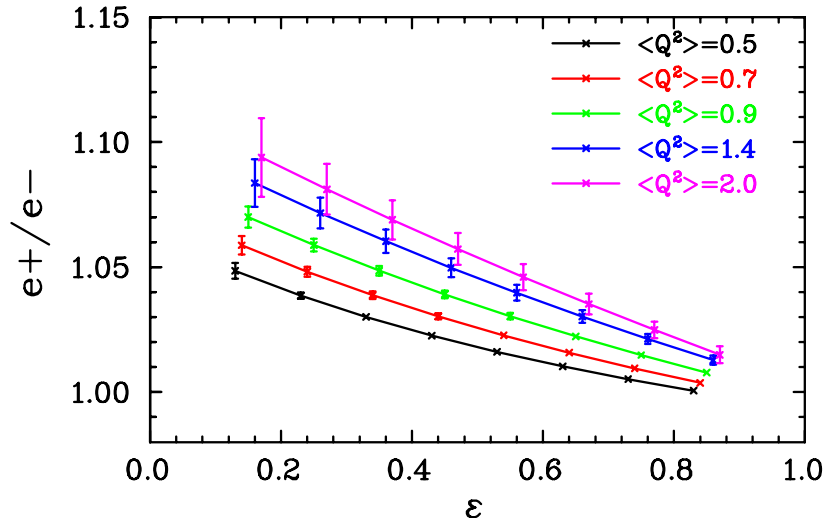


FIG. 41: Projected results and uncertainties for the positron-to-electron ratio. The error bars on the points are the statistical uncertainties, the systematic uncertainty is expected to be less than 1%.

obtained from the CLAS data. This would in turn greatly strengthen our understanding of the role of the two-photon exchange in the elastic scattering process, and may resolve the currently dilemma concerning the discrepancy between the Rosenbluth-method analysis and the polarization analysis.

Figure 41 shows the projected results for the positron to electron ratio for several Q^2 bins. The size of the projected two-photon effects is based on the analysis from Ref. [10] described in Sec. IIIB 2. Figure 42 show the ε -dependence for each Q^2 bin, based on a linear fit to the points in Fig. 41. The outer error bars in Fig. 41 are calculated assuming a worst case scenario of 1% uncorrelated systematic uncertainty at every ε point. We expect systematic uncertainties to be below 1%, especially for the low ε values, where the difference in acceptance for positrons and electron is smaller. The hollow blue square in Fig. 42 indicates the ε -dependence of the TPE effect on the cross section as estimated from a combined analysis of all previous positron data [19]. Hadronic calculations of the TPE effect, including only the intermediate elastic state, yield similar predictions for large Q^2 values, but show a more rapid decrease with decreasing Q^2 , with TPE effects going to zero in the vicinity of 0.3–0.4 GeV².

VI. EXPERIMENTS WITH SIMILAR PHYSICS GOALS

There are many experiments that have been proposed to look at two-photon exchange. There have been several proposals to look at polarization observables in e - N elastic scattering that are zero in the Born approximation, one of which was approved using a polarized ^3He target as a effective neutron target [40]. While these are very sensitive to TPE effects, they are not sensitive to the real part of the TPE amplitude that directly affects the extraction of the form factors. While these measurements do not directly relate to the difference in the electron- and positron-proton cross sections, nor to the form factor measurements, they do provide entirely independent measurements of TPE effects, and so are complementary to the measurements proposed here for testing models of TPE effects. The same is true of existing [25, 26] and future measurements of beam normal asymmetries, which provide direct measurements of TPE effects, but do not constrain the effects of TPE on the polarization or Rosenbluth separation

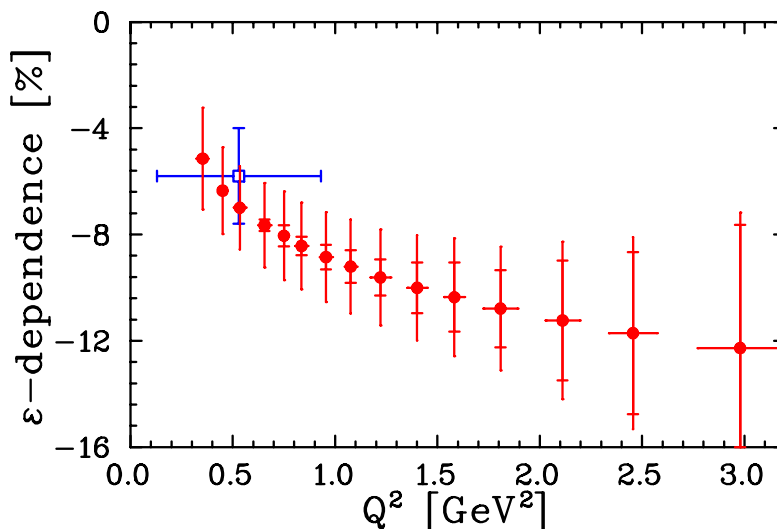


FIG. 42: Slope (ϵ -dependence) as a function of Q^2 , based on a linear fit to the projected results. Inner error bars are based on the statistical uncertainty, outer error bars include the effect of a 1% systematic uncertainty for each ϵ point, which is an overestimate of the final uncertainty we expect (see text). The blue square is the ϵ -dependence as determined from existing positron data.

form factor measurements.

There have been two experiments approved at Jefferson Lab that are directly sensitive to the real part of the TPE amplitudes. Experiment E04-019 was approved by PAC25 to measure the ϵ -dependence of polarization transfer measurements. This is sensitive to the ϵ -dependence of the two-photon amplitude $Y_{2\gamma}$ as defined in Ref. [9], which is important because the ϵ -dependence of the unpolarized cross section comes from a combination of TPE amplitudes, and another observable must be used to separate the ϵ -dependence of the amplitudes. Because the experiment will determine the ϵ -dependence but not the *size* of $Y_{2\gamma}$, it will not by itself provide enough information to correct the polarization transfer results for two-photon effects.

E05-017 was approved to study two-photon effect by making precise Rosenbluth measurements to check the linearity of the reduced cross section and to make precise measurements of the form factor ratio G_E/G_M . It is designed to look for non-linear terms coming from two-photon effects and to precisely measure the discrepancy to extract the size of the two-photon effects at large Q^2 . Precise Rosenbluth extractions over a range in Q^2 will provide detailed information on the discrepancy between Rosenbluth and polarization measurements, which puts significant constraints on the form of the TPE effects, assuming that they are fully responsible for the difference. The precise measurements of the ϵ -dependence of the unpolarized cross section can be combined with the measurements of the ϵ -dependence in the polarization transfer measurements to help disentangle the effect of the different TPE amplitudes on the form factor measurements, which is important in constraining the effect of TPE on polarization measurements.

Both of these experiments provide important information on TPE effects, but neither provides a clean measurement of TPE effects, and one must assume that TPE effects fully explain the discrepancy to use these results to correct the form factor measurements. While this appears to be a reasonable assumption, only the direct measurements of TPE, provided by the proposed positron measurements, can directly verify this assumption and provide a direct extraction of TPE effects. While the proposed measurements are limited to moderate Q^2 values, verification

of TPE effects as the source of the discrepancy will allow a clean interpretation of the high- Q^2 Rosenbluth measurements in terms of TPE effects, allowing measurements of the effects of TPE up to much larger Q^2 values. Therefore, the positron measurements, which provide direct information at low-to-moderate Q^2 values, and the measurements of the ε -dependence of the cross section and polarization transfer at larger Q^2 values, provide important complementary measurements of the effects of TPE.

VII. CONCLUSIONS

There are indications that two-photon exchange corrections may be responsible for the discrepancy between Rosenbluth and polarization transfer measurements of the proton form factors. Calculations of these effects are incomplete and existing positron measurements are limited to $Q^2 \approx 0.5 \text{ GeV}^2$ and yield only a weak (three sigma) indication of a ε -dependence. Additional measurements are necessary to establish TPE corrections as the source of the discrepancy.

These proposed measurements of the ratio of electron- to positron-proton elastic scattering will allow us to directly determine the TPE contribution to the cross section for $0.5 < Q^2 < 2 \text{ GeV}^2$ and $0.1 < \varepsilon < 0.9$. In this region we will make a precise determination of the ε -dependence of the TPE contributions, which can be used to test models of the TPE corrections. At higher Q^2 values, up to 3 GeV^2 , we will measure the Q^2 -dependence of the corrections, and determine the approximate ε -dependence. With this data, we can make a model-independent TPE correction to existing Rosenbluth extractions of G_E and G_M up to $Q^2 \approx 2 - 3 \text{ GeV}^2$. This data will allow us to determine if two-photon exchange corrections fully explain the discrepancy between the values of G_E extracted by the Rosenbluth and polarization transfer measurements.

There are two possibilities:

1. We confirm that TPE are responsible for the observed difference between Rosenbluth and polarization transfer measurements. Our measurements will be used to constrain calculations of TPE. In addition, measurements of the Rosenbluth/polarization transfer discrepancy itself can then be used to extend these studies of the two-photon effects to larger Q^2 .
2. We determine that the TPE corrections do *not* explain the form factor discrepancy. Then the explanation for the striking difference between Rosenbluth and polarization transfer measurements must be found elsewhere.

Either way, this proposed experiment will have very exciting results.

-
- [1] L. Andivahis et al., Phys. Rev. D **50**, 5491 (1994).
 - [2] M. K. Jones et al., Phys. Rev. Lett. **84**, 1398 (2000).
 - [3] O. Gayou et al., Phys. Rev. Lett. **88**, 092301 (2002).
 - [4] J. Arrington, Phys. Rev. **C68**, 034325 (2003).
 - [5] M. E. Christy et al., Phys. Rev. C **70**, 015206 (2004).
 - [6] I. A. Qattan et al., Phys. Rev. Lett. **94**, 142301 (2005), nucl-ex/0410010.
 - [7] C. Alexandrou, G. Koutsou, J. W. Negele, and A. Tsapalis, Phys. Rev. **D74**, 034508 (2006).
 - [8] D. H. Beck, Phys. Rev. **D39**, 3248 (1989).
 - [9] P. A. M. Guichon and M. Vanderhaeghen, Phys. Rev. Lett. **91**, 142303 (2003).
 - [10] J. Arrington, Phys. Rev. C **71**, 015202 (2005).

- [11] J. Arrington, Phys. Rev. **C69**, 022201 (2004).
- [12] V. Tvaskis et al., Phys. Rev. **C73**, 025206 (2006).
- [13] P. E. Bosted, Phys. Rev. C **51**, 409 (1994).
- [14] P. G. Blunden, W. Melnitchouk, and J. A. Tjon, Phys. Rev. Lett. **91**, 142304 (2003).
- [15] Y. C. Chen, A. Afanasev, S. J. Brodsky, C. E. Carlson, and M. Vanderhaeghen, Phys. Rev. Lett. **93**, 122301 (2004).
- [16] S. Kondratyuk, P. G. Blunden, W. Melnitchouk, and J. A. Tjon (2005), nucl-th/0506026.
- [17] A. V. Afanasev, S. J. Brodsky, C. E. Carlson, Y.-C. Chen, and M. Vanderhaeghen, Phys. Rev. **D72**, 013008 (2005).
- [18] P. G. Blunden, W. Melnitchouk, and J. A. Tjon, Phys. Rev. **C72**, 034612 (2005).
- [19] J. Arrington, Phys. Rev. **C69**, 032201 (2004).
- [20] M. N. Rosenbluth, Phys. Rev. **79**, 615 (1950).
- [21] E. Offermann et al., Phys. Rev. C **44**, 1096 (1991).
- [22] G. Fricke et al., Phys. Rev. C **45**, 80 (1992).
- [23] N. Voegler et al., Phys. Rev. C **43**, 2172 (1991).
- [24] P. Gueye et al., Phys. Rev. **C57**, 2107 (1998).
- [25] S. P. Wells et al. (SAMPLE), Phys. Rev. **C63**, 064001 (2001).
- [26] F. E. Maas et al., Phys. Rev. Lett. **94**, 082001 (2005).
- [27] Y. S. Tsai, Phys. Rev. **122**, 1898 (1961).
- [28] L. W. Mo and Y.-S. Tsai, Rev. Mod. Phys. **41**, 205 (1969).
- [29] L. C. Maximon and J. A. Tjon, Phys. Rev. **C62**, 054320 (2000).
- [30] S. D. Drell and J. D. Sullivan, Phys. Lett. **19**, 516 (1965).
- [31] A. Afanasev, S. Brodsky, and C. Carlson, presented at the DNP Meeting, Tuscon, AZ, Oct. 2003.
- [32] J. Mar et al., Phys. Rev. Lett. **21**, 482 (1968).
- [33] Y. S. Tsai, Tech. Rep., SLAC Report (1971).
- [34] W. R. Nelson, T. M. Jenkins, R. McCall, and J. K. Cobb, Phys. Rev. **149**, 201 (1966).
- [35] V. A. Batarin et al., Nucl. Instr. Methods **A 510**, 248 (2003).
- [36] P. L. Mattern, IEEE Trans. Nucl. Sci. **NS-21**, 81 (1974).
- [37] P. Degtyarenko, Proceedings of the Second Specialist's Meeting on Shielding Aspects of Accelerators, Targets and Irradiation Facilities (**SATIF2**), **12-13 October 1995, CERN, Geneva, Switzerland**, 67 (1995).
- [38] P. Degtyarenko, M. Kossov, and H.-P. Wellisch, Eur. Phys. J. **A 8**, 217 (2000).
- [39] B. Mecking et al., Nucl. Instr. Methods **A 503/3**, 513 (2003).
- [40] T. Averett, J. P. Chen, X. Jiang, et al., Jefferson lab proposal E05-015.
- [41] courtesy of Pavel Degtiarenko, author of GDINR
- [42] See logs for runs 41708 and 41709.